Retrieval of microphysical properties of dust aerosols from extinction, backscattering and depolarization lidar measurements using various particle scattering models

Yuyang Chang[1], Qiaoyun Hu[1], Philippe Goloub[1], Thierry Podvin[1], Igor Veselovskii[2], Fabrice Ducos[1], Gaël Dubois[1], Masanori Saito[3], Anton Lopatin[4], Oleg Dubovik[1], and Cheng Chen[5,6]

[1] Univ. Lille, CNRS, UMR 8518–LOA–Laboratoire d'Optique Atmosphérique, Lille 59650, France
[2] Prokhorov General Physics Institute of the Russian Academy of Sciences, Moscow, Russia
[3] Department of Atmospheric Science, University of Wyoming, Laramie 82071, WY, USA
[4] GRASP–SAS, Remote Sensing Developments, Lille 59650, France
[5] Anhui Institute of Optics and Fine Mechanics, Hefei Institutes of Physical Science, Chinese Academy of Sciences, Hefei 230031, China
[6] Key Laboratory of Optical Calibration and Characterization, Anhui Institute of Optics and Fine Mechanics, Chinese Academy of Sciences, Hefei 230031, China

Correspondence to: Qiaoyun Hu (qiaoyun.hu@univ-lille.fr)

Abstract Mineral dust is a key atmospheric aerosol agent that impacts the radiation budget and plays a significant role in cloud formation. However, studies on retrieving height-resolved microphysical properties of dust aerosols, which are crucial for understanding dust evolution and transport processes, from lidar measurements are still insufficient. Here, we retrieve dust aerosol microphysical properties, including the volume size distribution, volume concentration, effective radius (r_{eff}), refractive index and single-scattering albedo, from spectral extinction, backscattering and depolarization lidar measurements. We evaluate the performance of three particle scattering models – Sphere, Spheroid and Irregular–Hexahedral (IH) models in terms of mimicking dust optical properties and deriving retrieval results. We also explore the influence of inverting different measurement sets, namely the conventional 3β (backscattering coefficients at 355, 532 and 1064 nm) + 2α (extinction coefficients at 355 and 532 nm) and the expanded $3\beta + 2\alpha + 3\delta$ (depolarization ratio at 355, 532 and 1064 nm) measurements, on the retrieval. Both simulations and inversions of real lidar measurements show that it is necessary to use non-spherical models and incorporate 3δ measurements to improve the retrieval accuracy. An increase of discrepancy in depolarization ratio produced by the IH and Spheroid models is observed for $r_{\mathrm{eff}} > 0.5\,\mu\mathrm{m}$, resulting in larger retrieval difference between the two non-spherical models after the inclusion of 3δ. The study demonstrates the prospect of retrieving height-resolved dust microphysical properties from lidar measurements, as well as potential limitations of the prevailing scattering models in simulating particle backscattering properties.

1 Introduction

Due to its annual emission and residence time, mineral dust is the most abundant aerosol species that impacts the Earth system in various aspects and scales. It directly modulates the Earth radiation budget by scattering and absorbing atmospheric radiation (Miller and Tegen, 1998), and in an indirect way by taking part in cloud formation (Ansmann et al., 2019; Bangert et al., 2012; DeMott et al., 2003; Rosenfeld et al., 2001; Seifert et al., 2010). Additionally, it contributes to ecosystem dynamics and biogeochemistry during cycling processes (Miller et al., 2004; Yu et al., 2015). Moreover, the occurrence of intense dust outbreaks reduces visibility, posing potential hazards for transportation and outdoor activities. Long-term exposure to dense dust aerosols harms human health, causing respiratory issues and cardiovascular diseases (Giannadaki et al., 2014). Therefore, it is crucial to monitor and retrieve the distribution and properties of dust aerosols so as to enhance our understanding of their role in the Earth system, and their impact on human society.

The light detection and ranging (lidar) is a unique technique for obtaining vertically resolved information on dust aerosols. Optical properties measured by state-of-the-art lidars, such as lidar ratio (LR), particle linear depolarization ratio (PLDR) and fluorescence, have been used to identify and distinguish dust aerosols from others (Burton et al., 2012; Nicolae et al., 2018; Veselovskii et al., 2022). Nevertheless, quantitative retrievals of microphysical properties of dust aerosols, such as the size distribution and complex refractive index (CRI) from lidar measurements remains challenging and limited. This is partly due to the shortage of applicable scattering models that precisely describe the backscattering properties of large non-spherical particles. It has been revealed by a number of investigators that the Lorenz–Mie theory for spherical particles is unable to reproduce the laboratory-measured flat phase function of dust particles for sideward and quasi-backward directions (Nakajima et al., 1989; Volten et al., 2001). The Spheroid model, which is a well-accepted non-spherical scattering model used in AERONET retrieval (Dubovik et al., 2006; Holben et al., 2006), however, might also encounter difficulties in simulating backscattering due to computational accuracy issues or limitation in considering the impact of complex morphology of highly irregular particles (e.g., Huang et al., 2023; Saito and Yang, 2023).

To date, only a limited number of studies have been conducted to retrieve dust aerosols from lidar measurements. The initial work by Veselovskii et al. (2010) combined the Spheroid model with regularization inversion of 3β (backscattering coefficients at 355, 532 and 1064 nm) + 2α (extinction coefficients at 355 and 532 nm) measurements. The authors also examined the impact of other factors on retrievals, such as the spectral dependence of the CRI and the inclusion of depolarization at 355 nm in the inversion dataset. Müller et al. (2013) utilized both the Sphere and Spheroid models to invert measurements acquired during the SAMUM campaign, and subsequently compared the results with AERONET retrievals and in situ measurements. Tesche et al. (2019) conducted case studies to investigate the effect of employing different combinations of depolarization measurements as input for the inversion of lidar optical data into dust aerosol microphysical properties. These studies highlight the significance of considering the non-sphericity of dust particles and the potential of acquiring height-resolved dust microphysical properties with lidar. However, there remains a lack of comprehensive simulation studies to more understand the limitations of different scattering models for lidar-aerosol retrieval, as well as the extent of improvement when

incorporating depolarization data. The following issues are currently in need of further investigation: (1) considering that the limited sensitivity of $(3\beta + 2\alpha)$ measurements to the size distribution of large particles has been acknowledged in spherical

65   aerosol retrieval (Chang et al., 2022), is it still the case for dust retrieval? Can it be ameliorated by incorporating depolarization measurements? (2) How accurately do the retrievals derived with different scattering models reproduce the lidar measurements? (3) Could the Spheroid model be the optimal choice if there are other non-spherical models available?

Recently, a new particle scattering model, known as the Irregular–Hexahedral (IH) model, aiming to mimic light scattering of large irregular-shaped particles such as mineral dust and volcanic ash has been proposed and developed by Saito et al. (2021)

70   and Saito and Yang (2021). Compared to the Spheroid model, the IH model utilizes more realistic shapes to represent dust morphology and exploits advanced computational methods to improve the accuracy towards 180° scattering direction by incorporating a coherent backscattering enhancement effect (Borovoi et al., 2013) However, there is a lack of research that applies the IH model to lidar data inversion, and compares the IH model with other applicable scattering models (such as the Sphere and Spheroid models) in order to better understand its strengths and limitations in terms of lidar–aerosol retrieval.

75   To address these issues, we conducted comprehensive simulations and real case studies using the Basic algOrithm for REtrieval of Aerosol with Lidar (BOREAL) algorithm, which allows an investigation of different scattering models for simulating aerosol optical properties (forward calculation) and retrieving aerosol microphysical properties (inverse process) (Chang et al., 2022). We aim to investigate the performance of the Sphere, Spheroid and IH models in retrieving dust aerosols from lidar measurements, and examine the impact of incorporating spectral depolarization on the retrieval results. Section 2 provides a

80   brief overview of the BOREAL algorithm, the used scattering models, the lidar system, and a summary of dust properties reported in previous literature. Section 3 presents comparisons of optical properties simulated with the scattering models. Sections 4 and 5 showcase retrievals derived by inversion of synthetic optical data and real measurements, respectively. Discussions are presented in Sect. 6, followed by conclusions in Sect. 7.

2 Methodology

85   ### 2.1 BOREAL algorithm

Considering an ensemble of poly-dispersed, randomly oriented aerosol particles of which each single particle follows the independent scattering process (Mishchenko et al., 2002), the extinction coefficient, α, and the element at the i-th line, j-th column of the phase matrix, denoted P_{ij}, can be respectively expressed as

$$\alpha(\lambda, m) = \int_{r_{\min}}^{r_{\max}} k_\alpha(\lambda, m, r) v(r) \mathrm{d}r \,, \tag{1}$$

90   $$P_{ij}(\lambda, m, \Theta) = \frac{1}{\sigma_{\text{sca}}(\lambda, m)} \int_{r_{\min}}^{r_{\max}} k_{ij}(\lambda, \Theta, m, r) v(r) \mathrm{d}r \,, \tag{2}$$

where $k_\alpha(\lambda, m, r)$ and $k_{ij}(\lambda, \Theta, m, r)$ are the kernels corresponding to the extinction and phase matrix elements, respectively, which are functions of the wavelength λ, the CRI ($m = m_{\text{R}} - im_{\text{I}}$), and the particle radius r (additionally, k_{ij} is also a function

of the scattering angle Θ). The volume size distribution (VSD) of the particle ensemble, $v(r)$, is a function of particle radius, and σ_{sca} is the scattering coefficient derived in a similar way as α.

95 From Eqs. (1–2), the backscattering coefficient, β, which describes the scattering intensity in the backward direction, and the PLDR, δ, which describes the ratio of the perpendicular-to-parallel polarization components of backscattered light, are given by

$$\beta(\lambda, m) = \frac{\sigma_{\text{sca}}(\lambda,m)P_{ij}(\lambda,m,\pi)}{4\pi}, \tag{3}$$

$$\delta(\lambda, m) = \frac{P_{11}(\lambda,m,\pi) - P_{22}(\lambda,m,\pi)}{P_{11}(\lambda,m,\pi) + P_{22}(\lambda,m,\pi)}, \tag{4}$$

100 respectively. It is well-demonstrated that $P_{11} \geq P_{22}$ and the equality holds for spherical particles (Mishchenko et al., 2002). Therefore, the PLDR is an indicator of particle sphericity, with $\delta \equiv 0$ for spheres and $0 < \delta < 1$ for non-spherical particles that are beyond the Rayleigh scattering regime.

To effectively retrieve aerosol microphysical properties from lidar measurements, the BOREAL algorithm was developed. A comprehensive explanation of the underlying principles and the implementation of BOREAL can be found in Chang et al.

105 (2022). Basically, the state vector, $\boldsymbol{x}$, composed of all aerosol microphysical properties of interest is linked with a measurement vector, $\boldsymbol{y}$, via the corresponding forward model, $\boldsymbol{f}$, and measurement error, $\boldsymbol{\varepsilon}$:

$$\boldsymbol{y}_1 = \boldsymbol{f}_1(\boldsymbol{x}) + \boldsymbol{\varepsilon}_1,$$
$$\boldsymbol{y}_2 = \boldsymbol{f}_2(\boldsymbol{x}) + \boldsymbol{\varepsilon}_2, \tag{5}$$
$$\boldsymbol{y}_3 = \boldsymbol{f}_3(\boldsymbol{x}) + \boldsymbol{\varepsilon}_3,$$

110 In BOREAL, three types of measurement vectors are considered: namely the lidar-measured optical properties, $\boldsymbol{y}_1$; the smoothing constraint on VSD, $\boldsymbol{y}_2$; and the a priori constraint on CRI. The last two equations of Eq. (5) are proposed to reduce the underdetermination and ill-posedness of the inverse system. The state vector is retrieved by solving the following multi-term non-linear least-square problem:

$$\arg\min\{\sum_{i=1}^{3}[\boldsymbol{y}_i - \boldsymbol{f}_i(\boldsymbol{x})]^T \mathbf{C}_i^{-1}[\boldsymbol{y}_i - \boldsymbol{f}_i(\boldsymbol{x})]\}, \tag{6}$$

115 where $\mathbf{C}_i$ is the measurement covariance matrix corresponding to $\boldsymbol{y}_i$.

For the sake of clarity and completeness, we briefly introduce the retrieval process of the algorithm. Firstly, a set of inversion windows, $[r_{\text{min}}, r_{\text{max}}]$, are defined. Each inversion window does not necessarily have overlapped regions with others and the union of all inversion windows covers the effective size domain (0.05–15 μm) where the measurements are considered to be sensitive to the state vector. For each inversion window, the corresponding individual solution to the state vector, consisting

120 of VSD represented by 8 log-equidistance size bins and wavelength-independent CRI, is retrieved by solving Eq. (6). Next, from all individual solutions, the qualified ones are selected by considering the fitting error and the shape of the VSD. Finally, the volume concentration (V_t), the effective radius (r_{eff}), and the single scattering albedo (SSA, denoted ϖ) of every selected individual solution are calculated. Together with the VSD and CRI, their statistical quantities (mean and standard deviation)

are output as the final solution for this retrieval. The elements of the state vector, as well as V_t, r_eff and ϖ, are referred to as

125   the state parameters of the particle ensemble.

Several modifications in BOREAL are made to fulfil the need of this study. Firstly, in addition to the conventional $(3\beta + 2\alpha)$ measurements, BOREAL is capable of inverting 3δ (PLDR at 355, 532 and 1064 nm) measurements; secondly, in addition to the Sphere model, two non-spherical models – the Spheroid and IH models (detailed description in Sect. 2.2), are integrated into the BOREAL's frame; and finally, BOREAL is improved to be able to consider the spectral variability of dust m_I.

130   **2.2 Scattering models for spherical and non-spherical particles**

In this study, three particle scattering models: the Sphere, Spheroid and IH models are adopted for simulating light-scattering by dust particles.

The Sphere model regards an aerosol particle as a sphere of which the scattering properties are calculated with the Lorenz–Mie theory. An ensemble of spherical particles is described by its size distribution. The Sphere model is widely adopted in the

135   fields of remote sensing (Dubovik and King, 2000; Levy et al., 2007; Müller et al., 1999), atmospheric aerosol modelling (Chin et al., 2002; Hess et al., 1998), radiative transfer calculation (Mayer and Kylling, 2005) and in situ measurements (Osborne et al., 2008). However, a number of studies have demonstrated that the Sphere model fails to accurately reproduce the scattering of dust particles whose shapes are far from spherical. An example of this is the inability of the Sphere model to represent the lidar-measured PLDR of non-spherical particles. Therefore, there is a pressing need of non-spherical models applicable to non-

140   spherical aerosol retrieval within the community.

The Spheroid model approximates an aerosol particle to a spheroid of which the shape is described by two parameters: the volume-equivalent radius, r_vol (the radius of the sphere having the same volume with the spheroid) and the axis ratio (the ratio of the spheroid rotational axis to the perpendicular axis). Thus, an ensemble of randomly oriented spheroids is characterized by the size and axis ratio distributions, which are thought of as independent of each other. For smaller size parameters, the

145   Spheroid model uses the advanced T-matrix method (Mishchenko et al., 2002) to calculate the scattering properties, while for larger size parameters, the approximate geometric-optics-integral-equation method (Yang and Liou, 1996) is utilized. The Spheroid model was proposed based on the fact that a spheroid is the simplest non-spherical shape with one more characteristic (axis ratio) compared to a sphere and the scattering of electromagnetic radiation by spheroids can be accurately simulated (Mishchenko and Travis, 1994). The study of Dubovik et al. (2006) showed that the Spheroid model can closely reproduce the

150   laboratory measurements of dust scattering matrices (Volten et al., 2001). The authors further found out that exploiting the Spheroid model in dust retrieval from AERONET measurements can effectively eliminate the artifact of an abnormally high fraction of the fine-mode VSD retrieved with the Sphere model, leading to a significant reduction in fitting errors. In the AERONET operational retrieval procedure (Holben et al., 2006), when only intensity measurements are inverted, the axis ratio distribution (ARD) is fixed to the one retrieved from the laboratory measurement of Volten et al. (2001) to reduce algorithmic

155   complexity. In this study, to avoid introducing too many unknown to the inversion system, we also fix the dust ARD as the same one employed by AERONET. Consequently, compared to spherical particles, no extra state parameters are introduced.

Although the Spheroid model shows superior performance to the Sphere model in mimicking the scattering of non-spherical particles, Dubovik et al. (2006) pointed out for large particles like mineral dust and large scattering angles (Θ > 175°), the accuracy deteriorates due to the limits of the approximate geometric-optics method. In this context, the IH model was recently proposed by Saito et al. (2021). An IH particle has the shape of a hexahedron with randomly tilted faces, characterized by the maximum diameter, D_{max} (the diameter of the circumscribed sphere of the particle), and the degree of sphericity. The IH model defines 20 IH particles with different sphericities and approximates an aerosol ensemble to being composed of the 20 IH particles with different mixing ratios. Thus, the characteristic of the whole ensemble is described by the size distribution and ensemble-weighted degree of sphericity, Ψ. To calculate the scattering properties, different methods are used depending on the size parameter: the Rayleigh scattering approximation for small size parameters, the invariant-imbedding T-matrix method (Bi et al., 2013; Johnson, 1988) for moderate size parameters and a combination of the geometric-optics-integral-equation method (Yang and Liou, 1996) and physical-geometric optics method (Yang et al., 2019) for large size parameters. Note that the differences between the invariant-imbedding T-matrix and advanced T-matrix methods are that the latter provides numeric exact solutions of electromagnetic scattering only for randomly orientated spheroids while the former for more general non-spherical particles. One noticeable feature of the IH model compared to the Spheroid model is that it improves the accuracy of calculating the coherent backscattering enhancement effect. As suggested by Saito et al. (2021) and Saito and Yang (2021), in practice, we fix Ψ to 0.71 for severely irregular particles (dust) retrieval. Accordingly, compared to spherical particles, no extra state parameters are introduced. In addition, to facilitate comparison with the Sphere and Spheroid models, we convert the scattering properties from functions of D_{max} to functions of r_{vol} via the effective volume of the IH particle ensemble which is provided by the model database.

2.3 Lidar system

In this study, BOREAL combined with different scattering models is applied to invert real dust optical properties measured by LILAS (LIlle Lidar AtmosphereS) – a multi-wavelength Mie-Raman-polarization-fluorescence lidar system developed by the Laboratoire d'Optique Atmosphérique, Université de Lille. LILAS exploits the Nd:YAG crystal to emit laser pulses with a repetition rate of 20 Hz and energy of 90, 100, 100 mJ at 355, 532, and 1064 nm. Currently, the receiving channels are composed of: 3 pairs of parallel- and cross-polarized channels at 355, 532, and 1064 nm for the reception of elastic signals, 3 Raman channels at 387, 408 and 530 nm and a broad band fluorescence channel centred at 466 nm. Such configuration allows simultaneous measurements of $3\beta + 2\alpha + 3\delta$ (PLDR at 355, 532, and 1064 nm) + $1\beta_F$ (fluorescence backscattering coefficient centred at 466 nm). Detailed descriptions of data acquisition and error analysis can be found in Hu (2018), Hu et al. (2019) and Veselovskii et al. (Veselovskii et al., 2020). LILAS can be transferred as an individual lidar instrument to perform measurements in field campaigns (Hu et al., 2020; Veselovskii et al., 2016), as well as make stationary routine aerosol observations at the ATOLL (ATmospheric Observation in LiLle) platform where various remote sensing and in situ instruments for atmospheric monitoring have been integrated into national and international observational networks such as EARLINET/ACTRIS and PHOTONS/AERONET (Holben et al., 1998; Wandinger et al., 2016).

2.4 A priori information on dust properties

Unlike certain aerosol species whose properties are highly variable depending on atmospheric conditions, such as hygroscopic or chemically active secondary aerosols, a number of studies have found commonalities in dust properties that could serve as a priori constraints in dust retrieval.

2.4.1 Size and morphology

Dust aerosols are mostly generated by wind erosion from arid soils (Alfaro et al., 1997). Dust aerosols freshly emitted by windblown processes contain considerable giant particles (with diameters lager than 20 μm), which do not remain airborne for long due to their high settling rate. In addition, a coarse mode with a diameter range between 0.8 and 10 μm is mainly generated from dust aggregates by saltation (Kok and Renno, 2009; Maring et al., 2003). Unlike the giant particles, these coarse-mode particles can steadily remain airborne and travel long distances, making them important constituents of mineral dust that have profound impacts on the climate (Tegen et al., 1996). Reid et al. (2008) found that the coarse-mode particle size distribution was primarily determined by the properties of soil sources rather than the wind speed. Their work also reported a global rough range of dust volume median diameter as ~3.5 ± 30% μm. They also pointed out that short to moderate transport distances have very little effect on the size distribution of coarse mode dust. However, for long-range transported dust (older than a week or longer than 1000 km), a shift towards smaller sizes and convergence into a more uniform size are expected due to the dust scavenging mechanisms (Uematsu et al., 1983). These findings have been verified by both remote sensing retrievals (Hu, 2018) and in situ measurements (Arimoto et al., 1997). Additionally, a fine mode of dust VSD was sometimes observed (d'Almeida and Schütz, 1983; Gomes et al., 1990). Although fine-mode dust has a persistent lifetime (Tegen and Lacis, 1996) and contributes significantly to aerosol optical depth (AOD) in the UV–VIS region (Kaufman et al., 2005), it is less abundant and less ubiquitous compared to coarse-mode dust (Reid et al., 2008). Gomes et al. (1990) attributed the formation of fine-mode dust to sandblasting of loose dust aggregates, which often occurs during dust storm periods characterized by high wind speeds. The non-sphericity of dust aerosols makes their optical properties, such as backscattering, depolarization ratio and degree of linear polarization, differ from spherical particles (comprehensive discussion will be given in Sect. 3). Scanning electron microscopic (SEM) images show that depending on size and composition, dust particles present diverse and complex morphology, such as platelets, irregular polyhedrons and aggregates (Gomes et al., 1990; Kandler et al., 2007; Reid et al., 2003).

2.4.2 Complex refractive index

The CRI of mineral dust is determined by its chemical composition and therefore related to the minerology of the soil. Kandler et al (2009) exploited X-ray diffraction analysis to identify silicates (feldspars and clay minerals), quartz, carbonates and iron-rich materials (hematite) as the main components of Saharan dust samples. They also found that, although the change of particle size affects the relative fractions of the components, this is not a major factor affecting dust CRI. Additionally, by analyzing

dust samples collected from 19 global sources, Di Biagio et al. (2019) found the average of the real part of the CRI (m_R), varied between 1.48 and 1.55 over the spectral range of 370-950 nm, showing no clear dependence either on wavelength or on the soil source. To the contrary, they found a strong spectral dependence of the imaginary part of the CRI (m_I), because of the existence of iron-rich materials which present strong absorption in the UV and much less absorption towards the VIS–NIR.

225 To study the spectral relationship of dust m_I for lidar wavelengths, we extrapolated or interpolated their published results. As shown in Fig. 1, the relationship between the imaginary part at 355 nm ($m_{I,355}$) and at 532 nm ($m_{I,532}$) can be approximated by a linear function, whereas the imaginary part at 1064 nm ($m_{I,1064}$) has a weak dependence on $m_{I,355}$ with a value around 0.001.
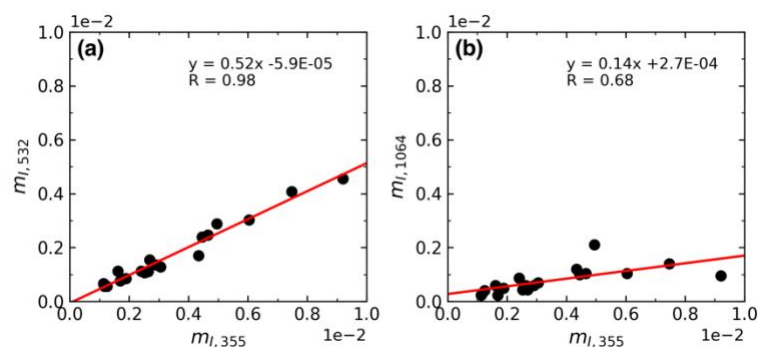
230 **Figure 1. Scatter plots and linear fitting of the spectral imaginary parts of CRI derived by interpolating or extrapolating the results published by Di Biagio et al. (2019): (a) imaginary parts at 355 and 532 nm; (b) imaginary parts at 355 and 1064 nm.**

Consolidated by these laboratory measurements, we modify the a priori constraints on CRI in BOREAL for dust retrieval in order to consider the spectral dependence of m_I. Specifically, spectrally independent m_R is retrieved with unmodified a priori constraints as used in Chang et al. (2022), while the $m_{I,355}$ is retrieved with the a priori value of 0.005 and the a priori standard

235 deviation of 0.005 (a detailed description about the a priori value and standard deviation can be found in Chang et al. (2022)). Then, $m_{I,532}$ is calculated from the relationship shown in Fig. 1, and $m_{I,1064}$ is fixed to 0.001. We believe taking account of the spectral dependence of the imaginary part of the CRI is essential in dust retrieval from lidar measurements because simulations suggest that ignoring it will lead to a retrieval error of 17-25% in V_t, as well as increases of retrieval uncertainty in other parameters (Veselovskii et al., 2010).

240 **2.4.3 Mixture with other aerosol types**

Dust particles could mix with other aerosol particles with higher sphericity so that the observed PLDR is lower than the pure case (Tesche et al., 2009). Previous studies related to dust retrieval from lidar measurements assumed the observed ensemble is a mixture of spherical and non-spherical parts which are of the same VSD and CRI but of different volume fractions. As a result, an additional state parameter, the spherical volume fraction (SVF), is introduced and retrieved (Müller et al., 2013;

245 Tesche et al., 2019; Veselovskii et al., 2010). Nevertheless, we have discovered that retrieving SVF greatly enlarges the system underdetermination, even when the spectral PLDR is incorporated into the inversion dataset. Moreover, we encounter

difficulties in determining the a priori constraints on the CRI of the aerosol mixture. Therefore, we exclude mixture cases and only work with pure dust retrieval in this study.

3 Optical properties simulated with the scattering models

250 To understand the differences of the Sphere, Spheroid and IH models in producing particle optical properties, as well as to investigate their sensitivity to the aerosol state parameters, bulk scattering properties are simulated based on lognormal VSD which is defined as

$$v(r) = \frac{1}{r} \frac{V_t}{\sqrt{2\pi} \ln S_g} \exp\left[-\frac{(\ln r - \ln r_v)^2}{2\ln^2 S_g}\right],$$ (7)

where r represents the particle radius for a spherical particle and volume-equivalent radius (r_{vol}) for a non-spherical particle.
255 In the parameterized lognormal VSD, r_V is the mode radius (or volume median radius), S_g the geometric standard deviation and V_t the volume concentration. The lognormal distribution has been widely used to represent the sizes of aerosols of different kinds in the fields of modelling, remote sensing and in situ measurements (Di Biagio et al., 2019; Dubovik et al., 2002; Hess et al., 1998; Whitby, 1978). The effective radius of a particle ensemble, r_{eff}, which is an important parameter to represent the overall size of the particle ensemble and is widely used in radiative transfer calculation (Chin et al., 2002; Hansen and Travis,
260 1974), is defined as

$$r_{eff} = \frac{\int_0^\infty v(r)\mathrm{d}r}{\int_0^\infty \frac{1}{r} v(r)\mathrm{d}r}.$$ (8)

Note that the work by Saito and Yang (2022) indicates that for random-orientated irregular particles, Eq. (8) is equivalent to the original concept of r_{eff} only if the effective radius of a single irregular particle is defined as $r_e = (3v)/(4a)$, where v and a are the volume and average projected area of that particle. For the moment, we uniquely use r_{vol} to calculate r_{eff} for both
265 spheroidal and IH particles, which leads to an acceptable overestimate (~10 − 20%) of r_{eff} (c.f., Fig. 1 of Saito and Yang, 2022). In the case of lognormal VSD, r_{eff} can be expressed as a function of r_v and S_g:

$$\ln r_{eff} = \ln r_v - \frac{1}{2}\ln^2 S_g .$$ (9)

We start with the comparison of angular scattering properties. Although for lidar measurements, we are only interested in the backward direction, such comparison is necessary to expand our understanding of the differences of the selected models in
270 simulating scattering properties of particles. It is also useful for the analyses of inversions of multi-angular measurements such as sun photometers measurements. Figure 2 shows phase matrix elements: P_{11}, P_{12} and P_{22} with respect to the scattering angle simulated with the IH, Spheroid and Sphere models, respectively. They are generated from a particle ensemble with: $r_v = 1.5\mu m$, $\ln S_g = 0.6$ (this leads to a r_{eff} of 1.25 μm, a value for typical transported dust aerosols (Hu, 2018)), $m_R = 1.5$, $m_I = 0.0015$ at 532 nm. The P_{12} and P_{22} are normalized to P_{11} while the P_{11} is normalized to its value at 30°. The phase function

275 (P_{11}) in the nearly forward direction is almost the same for spherical and spheroidal particles, and around twice as large for IH particles. This is explained by the larger average projected geometric area of the IH particles compared to the spherical and spheroidal particles with the same volume-equivalent radius, since the forward peak of the phase function is dominated by diffraction whose magnitude increases with increasing projected geometric area. Except the forward direction, both magnitudes and variations of the phase functions of spheroidal and IH particles are similar, particularly for $0 < \Theta < 60°$ where the values

280 of P_{11} are almost the same. This indicates the similarity of the inversions of the photometer sky measurements using the two non-spherical models. On the other hand, the scattering intensities of the non-spherical particles are dissimilar from those of spherical particles in side and backward directions. The enhancement of intensity in the backward direction of spheres is mainly due to the so-called surface wave on the particle caused by the edge rays (van de Hulst, 1957) and is a manifest feature different from non-spherical particles. Comparison of the degree of linear polarization ($-P_{12}/P_{11}$) reveals an opposite variation

285 between the spherical and non-spherical particles, indicating the difference in the vibrational direction of the polarized component. The polarization of non-spherical particles has a lower magnitude than that of spheres. Comparison of P_{22}/P_{11}, a parameter related to the PLDR via Eq. (4), not only highlights the contrast between the spheres and non-spherical particles, but also showcases the consistency in angular variation but the difference in magnitude between the spheroidal and IH particles. The difference of P_{22}/P_{11} in the backward direction between the spheroidal and IH particles is ~40%, indicating the difference

290 of inverting PLDR measurements using the Spheroid and IH models.
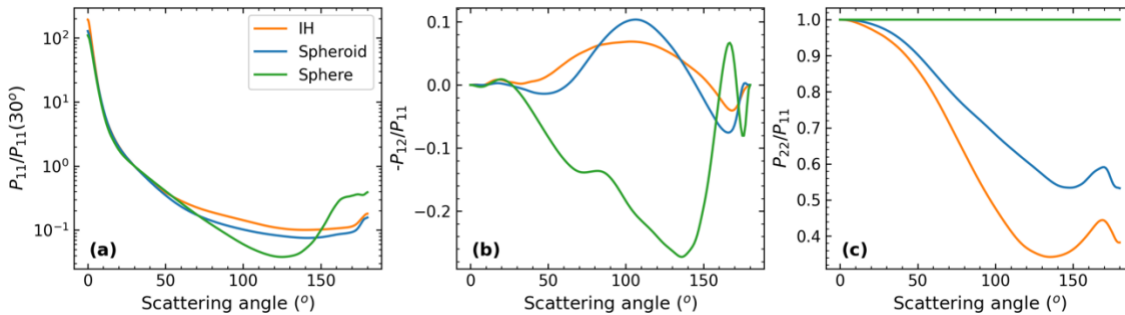
Figure 2. Normalized phase matrix elements: (a) $P_{11}/P_{11}(30°)$, (b) $-P_{12}/P_{11}$, (c) P_{22}/P_{11} with respect to the scattering angle. The calculation is done for 532 nm wavelength and a monomodal VSD with $r_v = 1.5\mu m$, $\ln S_g = 0.6$, and $m = 1.5 - i0.0015$ using the IH, Spheroid and Sphere models, respectively.

295 Figure 3 illustrates the variation of SSA with respect to the effective radius (r_{eff}) and the effective size parameter, $x_{eff} = 2\pi r_{eff}/\lambda$, for different CRIs simulated with the three scattering models at 532 nm, respectively. The $\ln S_g$ of the monomodal VSD is 0.6. The SSA displays distinct patterns for different size regions. For small r_{eff}, SSA is a monotonically increasing function of x_{eff} because according to the Rayleigh approximation, as x_{eff} grows, the scattering efficiency increases much faster than the absorption efficiency for a fixed CRI. As m_I rises, the upper r_{eff} (x_{eff}) bound of the Rayleigh region shifts towards

300 the right from ~0.02μm (~0.3) to ~0.07μm (~0.8). Beyond the Rayleigh region and with the continuous increase of particle size, the SSA reaches the maximum, stays, and subsequently decreases. However, note that it should be always greater than 0.5 as x_{eff} approaches to the geometric optics region due to the presence of the ray-tracing scattering cross section (Mishchenko

et al., 2002). The SSA shows strong sensitivity to m_I, a main contributor to the absorption efficiency factor, while it only presents limited sensitivity to m_R in the Rayleigh region. On the other hand, the SSA is little sensitive to particle shape for

305 particles with the same size, except for $r_{eff} > 0.6\mu m$ ($x_{eff} > 7$) and $m_I > 0.001$ where spheres produce lower SSA than spheroids and IH particles. This is consistent with the study by Saito and Yang (2022).
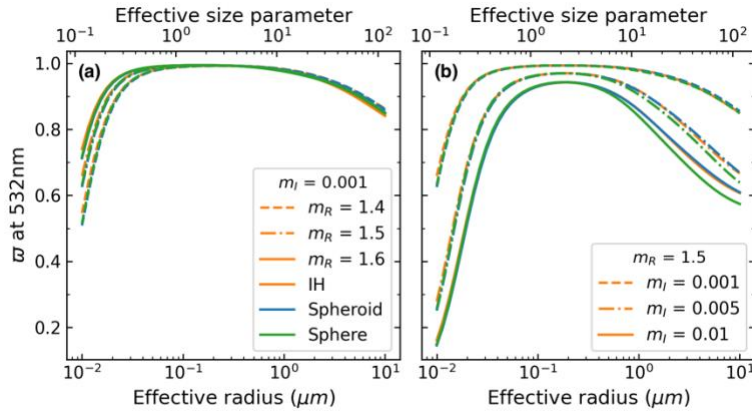
Figure 3. SSA (ϖ) at 532 nm simulated with the IH, Spheroid and Sphere models as functions of effective radius and effective size parameter for different CRIs:(a) m_I is fixed to 0.001 and the $m_R = 1.4, 1.5, 1.6$; (b) m_R is fixed to 1.5 and $m_I = 0.001, 0.005, 0.01$.
310 The VSDs used for the calculation have a geometric standard deviation of $\ln S_g = 0.6$.

Similar to Fig. 3, Fig. 4 displays the variations of lidar-measured properties – α, β, and δ simulated with the three scattering models with respect to r_{eff} (x_{eff}) for different CRIs at 532 nm. The VSD used has a $\ln S_g = 0.6$. Both α and β exhibit a "bridge" shape, namely first increase and then decrease with increasing r_{eff}. This is because on the one hand, as x_{eff} grows, the extinction and scattering efficiencies firstly increase up to the first interference peak and then decrease; on the other hand, the

315 total geometric cross-section which is proportional to the total surface area for convex particles (Vouk, 1948) decreases with the increase of r_{eff} because V_t is fixed to unity. The extinction coefficient shows little dependence on m_I within the considered range ($0.001 \leq m_I \leq 0.01$). However, its sensitivity to m_R varies depending on the range of r_{eff}. The change of particle shape also brings little effect on α, except for the vicinity of the maximum extinction where the α of IH particles is slightly smaller than those of spheres and spheroids. In contrast to extinction, the backscattering coefficient presents sensitivity to both m_R

320 and m_I (for $r_{eff} > 0.1\mu m$). In addition, under the same state parameters, the Sphere model can yield a β higher than the non-spherical models by a factor of 5 at most (the corresponding state is $r_{eff} = 2.8\mu m$, $m_R = 1.6$, $m_I = 0.001$). The PLDR generated by the two non-spherical models exhibit distinct dependence on the state parameters for different r_{eff} regions. When $r_{eff} < 0.5\mu m$, PLDR presents a clear positive correlation with r_{eff} and is little affected by the variations of CRI and particle shape. When $r_{eff} > 0.5\mu m$, however, the sensitivity of PLDR to the effective radius decreases while the sensitivity to the CRI

325 increases. Meanwhile, for $r_{eff} > 0.5\mu m$, the PLDRs generated by the IH and Spheroid models diverge from each other–the former is of an evidently higher value while the latter reaches the maximum between $r_{eff} = 0.8$ and $r_{eff} = 1$ μm, and then decreases. Moreover, note that there is a r_{eff} region (0.4–0.6 μm for the Spheroid model, 0.7-1.5 μm for the IH model) after which the sensitivity of PLDR to m_R switches from positive to negative.
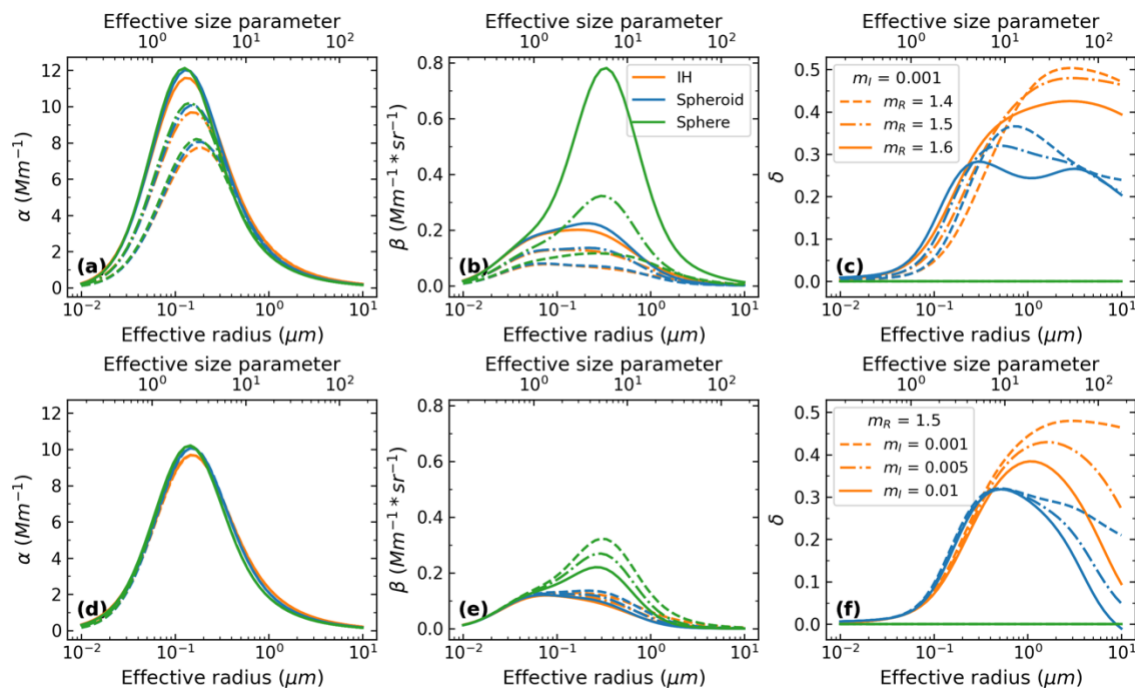
Figure 4. Same as Fig. 3 but for (a, d) extinction coefficient (α), (b, e) backscattering coefficient (β) and (c, f) PLDR (δ). The m_I is fixed to 0.001 and m_R varies in the top row (a–c), while the m_R is fixed to 1.5 and m_I varies in the bottom row (d–f).

To further study the sensitivities of lidar measurements to particle CRI, Figs. 5 and 6 show variations of α, β and δ at 532 nm with respect to m_R and m_I for the three scattering models, respectively. We utilized the same VSD parameters as those to generate Fig. 2 (i.e., $r_V = 1.5\mu m$, $r_{eff} = 1.25\mu m$) and calculated the optical properties for discrete values of m_I in Fig. 5, and discrete values of m_R in Fig. 6. It shows that α is neither sensitive to m_I nor m_R. For example, the largest reduction of α caused by the increase of m_R from 1.4 to 1.65 turns out to be 5% (and occurs for the Spheroid model), a value comparable to the measurement uncertainty and much less than the variation associated with the change of particle shape. For all the scattering models, β behaves as a monotonic increasing function of m_R and a monotonic decreasing function of m_I. The sensitivity of β to either m_R or m_I increases with the increase of m_R and decrease of m_I. Among the three models, the Sphere model produces the largest β dynamic with the change of m_R and m_I, while the two non–spherical models produce nearly the same values. Nevertheless, the PLDR exhibits significant shape-dependent characteristics: the PLDR produced by the Spheroid model presents a strong sensitivity to m_R but a weak sensitivity to m_I, while to the contrary, the PLDR produced by the IH model shows an obvious dependence on m_I but a relatively weak dependence on m_R. It is worth stressing that the PLDRs produced by the two non–spherical models present complex patterns with respect to CRI for $r_{eff} > 0.5\mu m$ (Fig. 4), while the result in Figures 5 and 6 is a zoom-in to $r_{eff} = 1.25\mu m$.
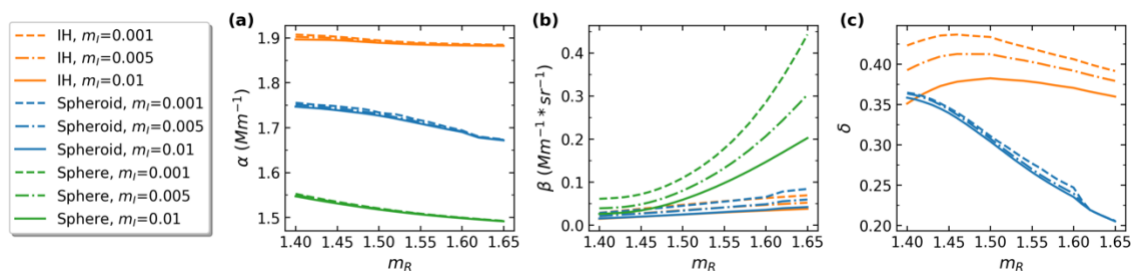
Figure 5. Variations of (a) α, (b) β, and (c) δ with respect to m_R for IH, Spheroid, and Sphere models and for $m_I = 0.001, 0.005$, and 0.01 at 532 nm, calculated from $r_V = 1.5\mu m$ and $\ln S_g = 0.6$.
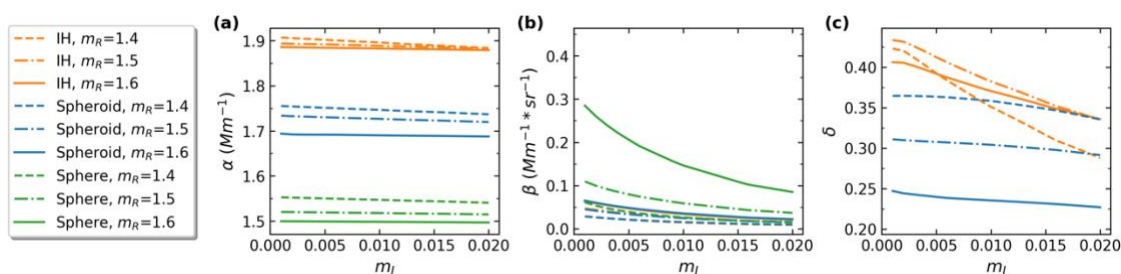
Figure 6. Same as Fig. 5 but the variations with respect to m_I for $m_R = 1.4, 1.5$, and 1.6.

Figure 7 displays the spectral variations of α, β and δ simulated with IH, Spheroid and Sphere models. The particle VSD is kept the same as that to generate Figs. 2, 5, 6 ($r_V = 1.5\mu m$, $\ln S_g = 0.6$). The spectral CRIs used for calculation are adopted from Table 4 in Di Biagio et al. (2019) and the values at lidar wavelengths are derived by linear interpolation or extrapolation. The dispersions of the values shown by shaded areas result from variation of the CRI. The extinction coefficients generated by the three models have similar spectral variations. Since the effective radius is fixed, the spectral variation of α is in accordance with the variation of the extinction efficiency which is a monotonic decreasing function of the effective size parameter in the considered size region and is smooth due to the averaging effect of size distribution (Bohren and Huffman, 2004). The backscattering coefficients first increase and then slowly decrease as the wavelength increases. Compared to the non-spherical particles, the spherical particles have a spectral β with a larger positive slope in the short-wavelength region, and more sensitive to the change of CRI. For the PLDR, however, the two types of non-spherical particles exhibit contrary spectral variations: a positive slope for spheroidal particles while a negative slope for IH particles, resulting in the largest PLDR difference in the UV.
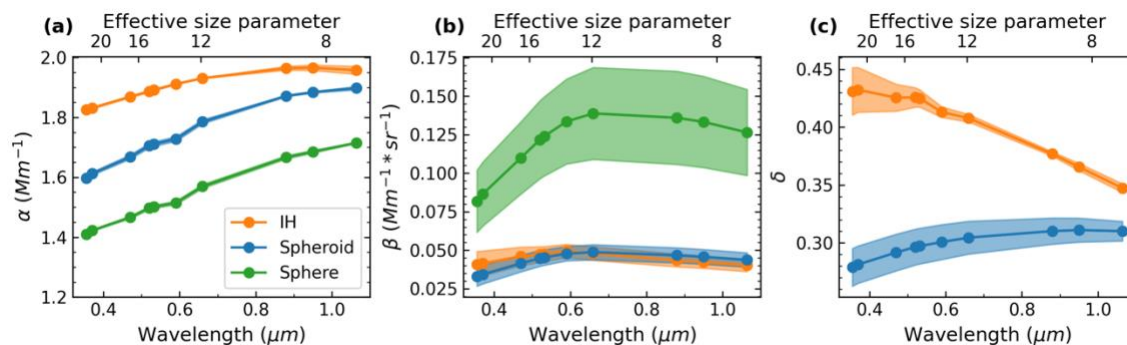
Figure 7. Spectral variations of (a) α, (b) β and (c) δ simulated with IH, Spheroid and Sphere models. The VSD for the calculation
has $r_V = 1.5\mu m$ and $\ln S_g = 0.6$. Spectral CRIs extracted from the Table 4 in Di Biagio et al. [2019] are used for the calculation
and the values at lidar wavelengths are derived by linear interpolation or extrapolation of the tabular CRIs. The means (solid lines)
and standard deviations (shaded areas) of the results are finally shown.

To further investigate the relationship between the spectral variation of lidar-measured optical properties and particle size, the
extinction Angstrom exponent (EAE) and backscattering Angstrom exponent (BAE) over 355 to 532 nm are shown in Figs. 8
and 9 as functions of r_{eff}. Definitions of EAE and BAE can be found in Hu et al. (2019). The $\ln S_g$ of the VSDs is 0.6. The m_I
is fixed to 0.01 in Fig. 8 and m_R is fixed to 1.5 in Fig. 9. As r_{eff} increases, EAE decreases swiftly from larger than 1.5 to
smaller than zero and then becomes flat, which means the extinction spectral variation is continuously small for $r_{eff} > 1\mu m$.
This variation is in line with the simulation by Schuster et al. (2006). The BAE overall shows a decreasing trend as r_{eff}
increases in spite of the complex pattern due to the changes of m_R and m_I. By contrast, the CRI has little influence on EAE,
particularly for large particles.
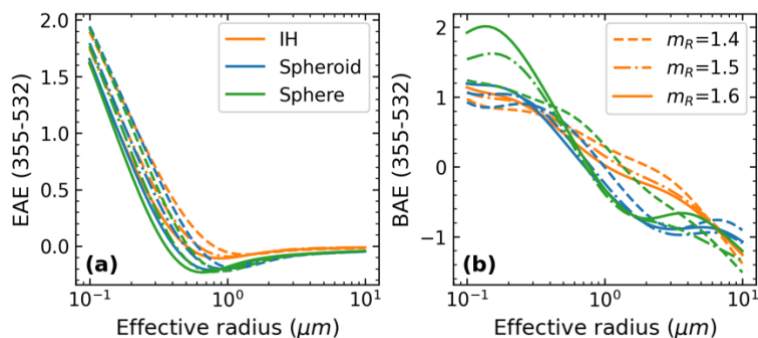
Figure 8. (a) Extinction Angstrom exponent (EAE) and (b) backscattering Angstrom exponent (BAE) with respect to effective radius
simulated with the IH, Spheroid, and Sphere models for $m_R = 1.4$, 1.5, and 1.6, respectively. The imaginary refractive index is fixed
to $m_I = 0.001$.
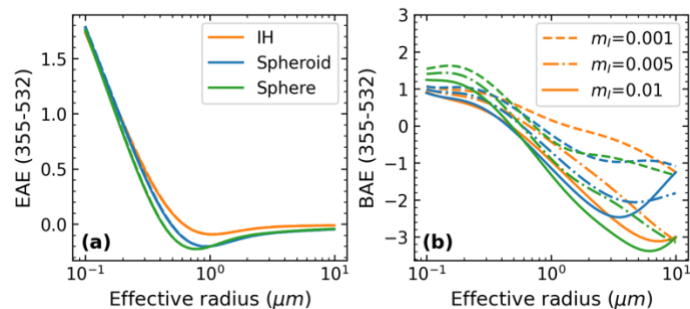
Figure 9. Same as Fig. 8 but simulated for $m_R = 1.5$ and $m_I = 0.001$, 0.005, and 0.01.

In conclusion, the aforementioned simulation illustrates the distinctions and resemblances among the Sphere, Spheroid and IH models in generating particle scattering properties. The backscattering coefficient is the most prominent contrast between the Sphere model and the non-spherical models, whereas the main difference between the two non-spherical models is observed in the PLDR.

4 Inversion of synthetic optical data

In this section, we study the performance of BOREAL in dust aerosol retrieval by inverting synthetic optical data calculated from predefined aerosol models in order to address the following questions. Namely, (1) given the state parameters of dust aerosols according to our a priori knowledge, are the scattering models capable of reproducing the ranges of real lidar measurements? (2) When different optical datasets (i.e., $3\beta + 2\alpha$ or $3\beta + 2\alpha + 3\delta$) are considered, how large is the spread of retrievals derived with the three scattering models (IH, Spheroid, Sphere)? (3) How dose measurement noise influence the retrieval accuracy?

4.1 Reproduction of lidar measurements and strategy of retrieval simulations

We define three VSDs to represent the size distributions of transported dust (TD), fresh dust (FD) and bimodal dust (BD, a mixture of fine–mode and coarse–mode dust). For CRI, three real parts and three imaginary parts are defined. The spectral dependence of the imaginary part is considered as described in Sect. 2.4.2. Hereinafter, unless explicitly stated, the imaginary part of CRI presented and discussed always refers to the monochromatic value at 355 nm, and for simplicity, the subscript "355" is omitted. Complete parameterization of the aerosol models is shown in Table 1, which leads to 27 sets of state parameters in total.

Table 1. Aerosol model setup for the retrieval simulation (subscript "f" for fine mode, "c" for coarse mode). The "Index of (m_R, $m_{I,355}$)" shows the CRI values corresponding to the x-axes in Figs. 11, 13, and 14.

Lognormal VSD (Eq. 6)
Transported dust (TD) $r_v = 1$ μm, $\ln S_g = 0.6$, $V_t = 1$, $r_{eff} = 0.84$ μm

Fresh dust (FD)	$r_v = 2$ μm, $\ln S_g = 0.6$, $V_t = 1$, $r_{eff} = 1.67$ μm								
Bimodal dust (BD)	$r_{v,f} = 0.13$ μm, $\ln S_{g,f} = 0.4$, $V_{t,f} = 0.1$, $r_{v,c} = 2$ μm, $\ln S_{g,c} = 0.6$, $V_{t,f} = 0.9$, $r_{eff} = 0.69$ μm								
Complex Refractive index (CRI)									
m_R	1.4, 1.5, 1.6								
$m_{I,355}$	0.001, 0.005, 0.009								
$m_{I,532}$	$0.52*k_{355}$ (see Sect. 2.2)								
$m_{I,1064}$	0.001								
	1	2	3	4	5	6	7	8	9
Index of (m_R, $m_{I,355}$)	(1.4, 0.001)	(1.4, 0.005)	(1.4, 0.009)	(1.5, 0.001)	(1.5, 0.005)	(1.5, 0.009)	(1.6, 0.001)	(1.6, 0.005)	(1.6, 0.009)

Figure 10 shows a comparison of dust intensive optical properties, i.e., LR, PLDR, $EAE_{355-532}$ and $BAE_{355-532}$ simulated with the scattering models and extracted from previous literatures (Floutsi et al., 2023; Haarig et al., 2022; Hu et al., 2020). The shaded areas for the simulations correspond to the dispersions due to the CRI variation while the error bars for the real
405 measurements mark the measurement errors provided by the literatures. Detailed values of the simulations and real measurements can be found in Table S1. Determined by the backscattering coefficient, the simulated LR shows strong sensitivity to CRI for all the scattering models. Generally, the values simulated with the Spheroid and IH models are similar and higher than the Sphere model because as mentioned, the Sphere model produces much higher β under the same aerosol condition. In spite of that, all three scattering models can reproduce the ranges of spectral LR measurements for the TD type.
410 For the FD and BD types, however, the Sphere model tends to underestimate LR at 532 and 1064 nm while the two non-spherical models are capable of well reproducing these values. It is worth mentioning that so far, we just found one published measurement of LR_{1064} for pure dust derived using the Raman technique (Haarig et al., 2022). For the reproduction of spectral PLDR, the Spheroid model generally performs better than the IH model for the TD and FD types, while the situation is reversed for the BD type. Furthermore, only the IH model can reproduce the "Haarig-22" PLDR at 1064 (when the TD type is assumed).
415 The simulated EAE and BAE shows obvious discrepancies with the measurements. The BAE comparison reveals that except for the TD type, all the scattering models tend to underestimate the BAE to different extent. For EAE, the TD and FD assumptions lead to all negative values while the BD assumption results in positive values that are too high compared to the measurements. Such discrepancies suggest that there might be certain limitations in these scattering models that preclude them from reproducing the measured EAE and BAE, although among the tested scattering models, the IH model provides the closest
420 results. Nonetheless, it is also possible that in reality, most dust aerosols are of bimodal VSDs with a variable fine mode, or the observed dust layers contain fine-mode pollutions, which result in the large dispersion of the EAE around zero compared to the monomodal simulation.
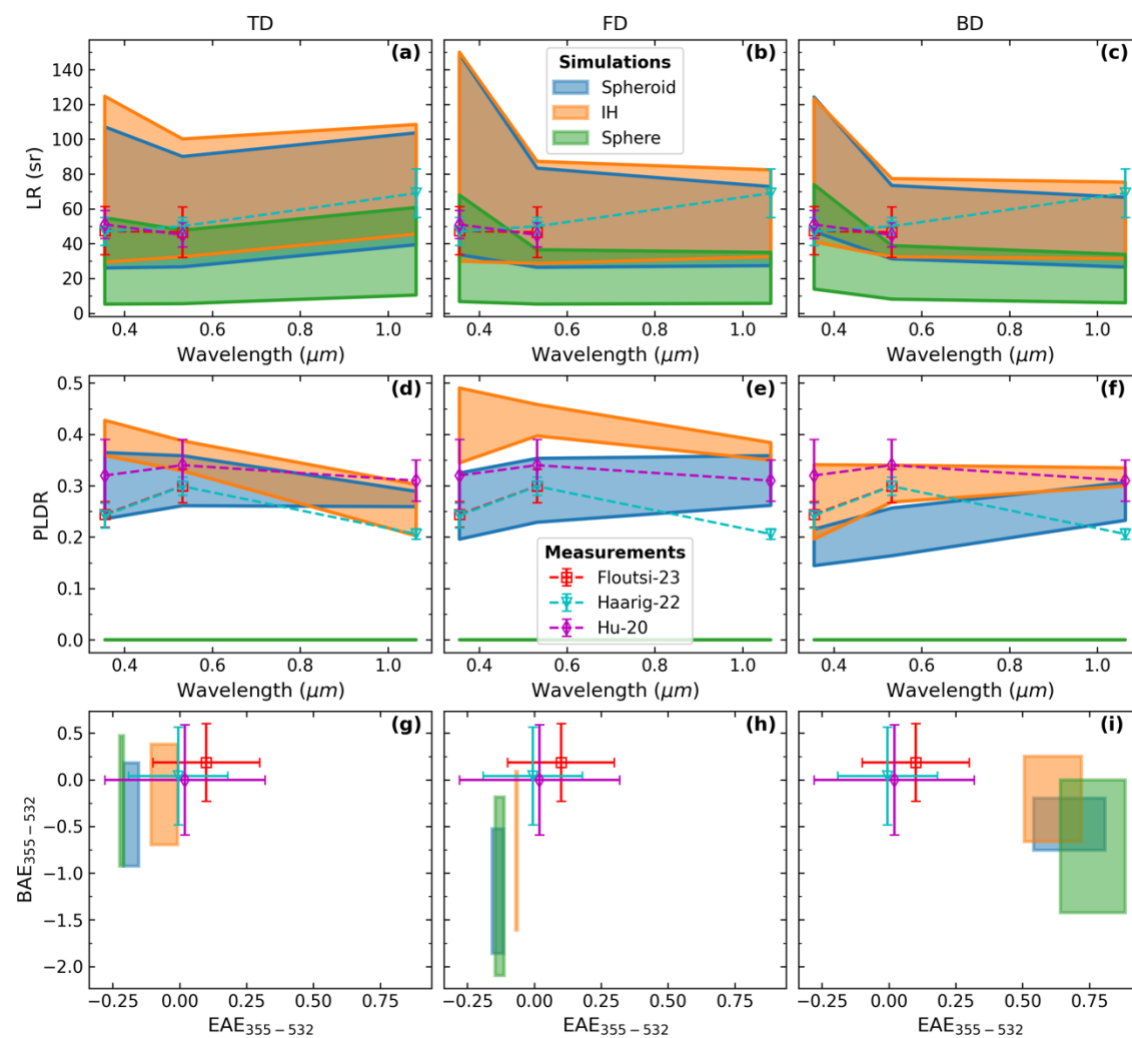
Figure 10. Spectral lidar ratio (LR) (a–c), PLDR (d–f), EAE and BAE (g–i) calculated from the aerosol models defined in Table 1
with the three scattering models, as well as extracted from the measurements reported by other literatures. The shaded areas for
different scattering models represent the dispersions of the simulation results due to CRI variation. The error bars for the real
measurements mark the measurement errors provided by the literatures. Among the measurements, Floutsi-23 combines the results
of Saharan, Central Asian and Middle Eastern dust reported by Floutsi et al. (2023); Haarig-22 corresponds to a pure dust case
reported by Haarig et al. (2022); and Hu-20 corresponds to the pure dust layer of the "Case 3" in Hu et al. (2020).

As mentioned, the main objective of the following retrieval simulations is to evaluate the influences of different retrieval configurations, including considerations of the three scattering models and two combinations of the input measurements (3β + 2α, 3β + 2α + 3δ), on the accuracy of the retrieval derived with BOREAL. To this end, firstly, optical datasets are calculated from the defined aerosol models using the Spheroid and IH models respectively to take into account dust non-sphericity. Next, the (3β + 2α + 3δ) and (3β + 2α) of the created optical datasets are inverted into state parameters using the three scattering models, respectively, with and without measurement noise. For clarity, in the following sections we separately compare the retrievals by the Sphere and IH models, the retrievals by the Spheroid and IH models, and the retrievals by the Sphere and IH

models considering measurement noise. Note that the comparison between the Sphere and Spheroid models leads to similar conclusions to that between the Sphere and IH models and thus is no longer presented here (see Fig. S1 in the Supplement).

To evaluate the performance of the retrieval of state parameters, the retrieval errors of V_t, r_{eff}, m_R, m_I and ϖ (monochromatic)

440 are defined as

$$\varepsilon(x) = \frac{\hat{x} - x^*}{x^*} \times 100\%, \quad (x = V_t, r_{eff}),$$ (10)

$$\varepsilon(x) = \hat{x} - x^*, \quad (x = m_R, m_I, \varpi),$$ (11)

respectively, where x^* and $\hat{x}$ represent the true and retrieved states, respectively. The root-mean-square error (RMSE) of ϖ over the wavelength is defined as

445 $$\varepsilon(\varpi)_{RMS} = \sqrt{\frac{1}{m} \sum_{i=1}^{m} (\hat{\varpi}_i - \varpi_i^*)^2},$$ (12)

where m is the number of the wavelengths at which ϖ is retrieved, and ϖ_i is the corresponding spectral value. Moreover, we use the fitting error as a metric to quantify how well the measurements are reproduced by the retrieval, which is defined as

$$\varepsilon_{fit} = \sqrt{\frac{1}{n} \sum_{i=1}^{n} \left(\frac{\hat{y}_i - y_i^*}{y_i^*}\right)^2} \times 100\%,$$ (13)

where n is the number of the measurements.

450 **4.2 Retrieval differences between the Sphere and IH models**

Figure 11 shows retrieval errors of V_t, r_{eff}, m_R, m_I, as well as fitting errors for the aerosol models in Table 1. The optical data are generated by the IH model without considering measurement noise and the results derived by inverting $(3\beta + 2\alpha + 3\delta)$ using the IH model, inverting $(3\beta + 2\alpha)$ using the IH model, and inverting $(3\beta + 2\alpha)$ using the Sphere model are shown, respectively. The x-axis in each panel corresponds to the CRI pairs specified in Table 1. When inverting the $(3\beta + 2\alpha)$ data

455 using the IH model, for low m_R^* and m_I^*, V_t and r_{eff} tend to be underestimated while m_R and m_I overestimated. Such a feature was also found for spherical particle retrieval from the $(3\beta + 2\alpha)$ data, which is caused by the cross-talk between state parameters and the influence of a priori constraints on CRI (Chang et al., 2022). The retrieved values of r_{eff} and V_t are positively correlated because from Fig. 4, for $r_{eff}^* > 0.5\mu m$, underestimation of r_{eff} leads to a reduction in both α and β, which in turn makes V_t increase to compensate for this reduction. The cross-talk between particle size and concentration was also

460 reported by Burton et al. (2016). The same analysis holds for m_R and m_I and the cross-talk is more significant since α has little sensitivity to CRI in the modelled size region. For instance, according to Figs. 5 and 6, a β_{532}^* value of 0.1 Mm^{-1}sr^{-1} can be produced either by $m = 1.5 - 0.001i$ or $m = 1.6 - 0.016i$ with the Sphere model. Incorporating spectral PLDR (3δ) into the inversion greatly improved the retrieval accuracy for all state parameters. This improvement agrees with the sensitivity study

in Sect. 3 which shows that spectral PLDR contains information on both particle size and CRI. Figure 11 also highlights that
465   using the Sphere model to retrieve non-spherical particles deteriorates the retrieval accuracy by either overestimating the
imaginary part (for $m_R^* = 1.4$) or underestimating the real part (for $m_R^* > 1.4$). This is because the spherical particle
assumption offsets β to higher values which have to be reduced by increasing m_I or decreasing m_R. Such retrieval bias resulting
from the use of the Sphere model to retrieve non-spherical particles was also observed in the study by Veselovskii et al. (2010),
where $m = 1.57 - 0.001i$ and the Spheroid model were used to generate the optical data.

470   Retrieval errors in SSA once again demonstrate that SSA is mostly dominated by m_I rather than m_R. The fitting errors are
generally less than 2%, much smaller than the maximum measurement error (10–20%) for a well-calibrated Mie–Raman–
depolarization lidar (Hu et al., 2019, 2020). It is worth mentioning that to avoid overfitting in a real retrieval, BOREAL is
designed to stop the iteration when the residual has the same order as the measurement noise (Chang et al., 2022). Therefore,
one can see the retrieval error is not zero even if the error-free optical data are inverted. However, an abnormal surge of ε_{fit} to
475   greater than 7% occurs for the BD type and $m_R^* = 1.6$ when the ($3\beta + 2\alpha$, IH) configuration is used.
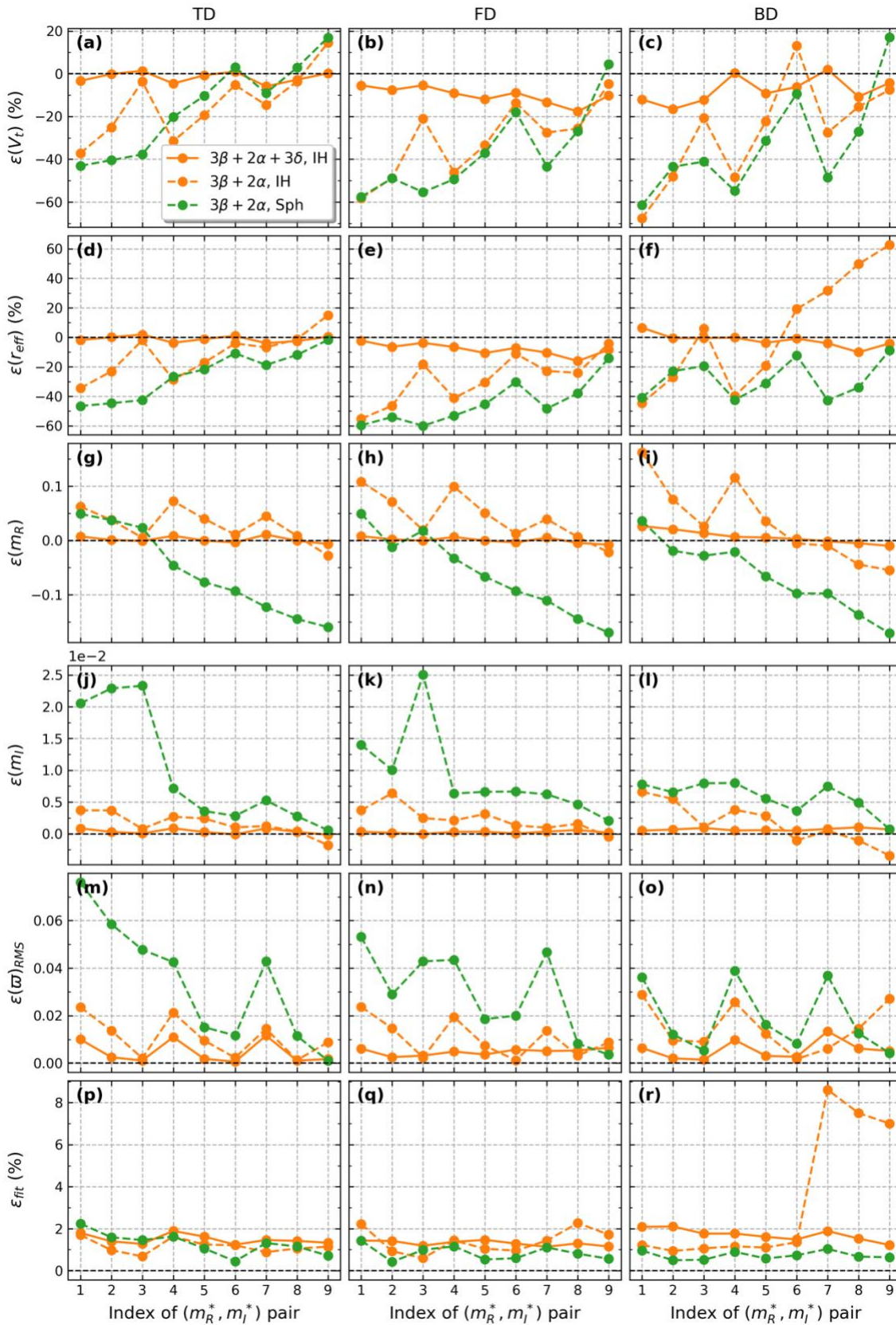
Figure 11. Relative retrieval errors of (a–c) V_t, (d–f) r_{eff} and absolute retrieval errors of (g–i) m_R, (j–l) m_I, (m–o) ϖ and (p–r) fitting error (ε_{fit}) by retrieving the aerosol models defined in Table 1 with different retrieval configurations: inversion of $3\beta + 2\alpha + 3\delta$ data using the IH model, inversion of $3\beta + 2\alpha$ data using the IH model, inversion of $3\beta + 2\alpha$ data using the Sphere model (Sph). The error-free synthetic optical data are generated by the IH model. The columns represent the VSD type of TD, FD and BD, respectively. The x–axis of each panel corresponds to the index of true CRI defined in Table 1.

480

To see if the retrieval configurations are able to derive correct features of particle size distribution, Fig. 12 visualizes the true and retrieved VSDs corresponding to the three VSD types (columns) and three true CRI states (rows). Consistent with Fig. 11, in most cases, retrieval accuracy diminishes with an increase in effective radius and the presence of the fine mode. The

485   inversion of ($3\beta + 2\alpha + 3\delta$) data yields the best retrieval accuracy of VSD even for the BD type, while the inversion of ($3\beta + 2\alpha$) data often underestimates r_V and V_t, which exacerbates with the decrease of m_R and m_I, the increase of r_{eff}, and the presence of the fine mode. On the other hand, the retrieval improves as m_R and m_I increase, except for the BD type retrieved with the ($3\beta + 2\alpha$, IH) configuration: as can be seen in Fig. 12(i), although the bimodal shape of the VSD is successfully retrieved, the total r_{eff} is highly overestimated due to an overestimate of the fine-mode r_{eff}, accompanied by an abnormal

490   increase of ε_{fit} (Fig. 11(f), 11(r)).
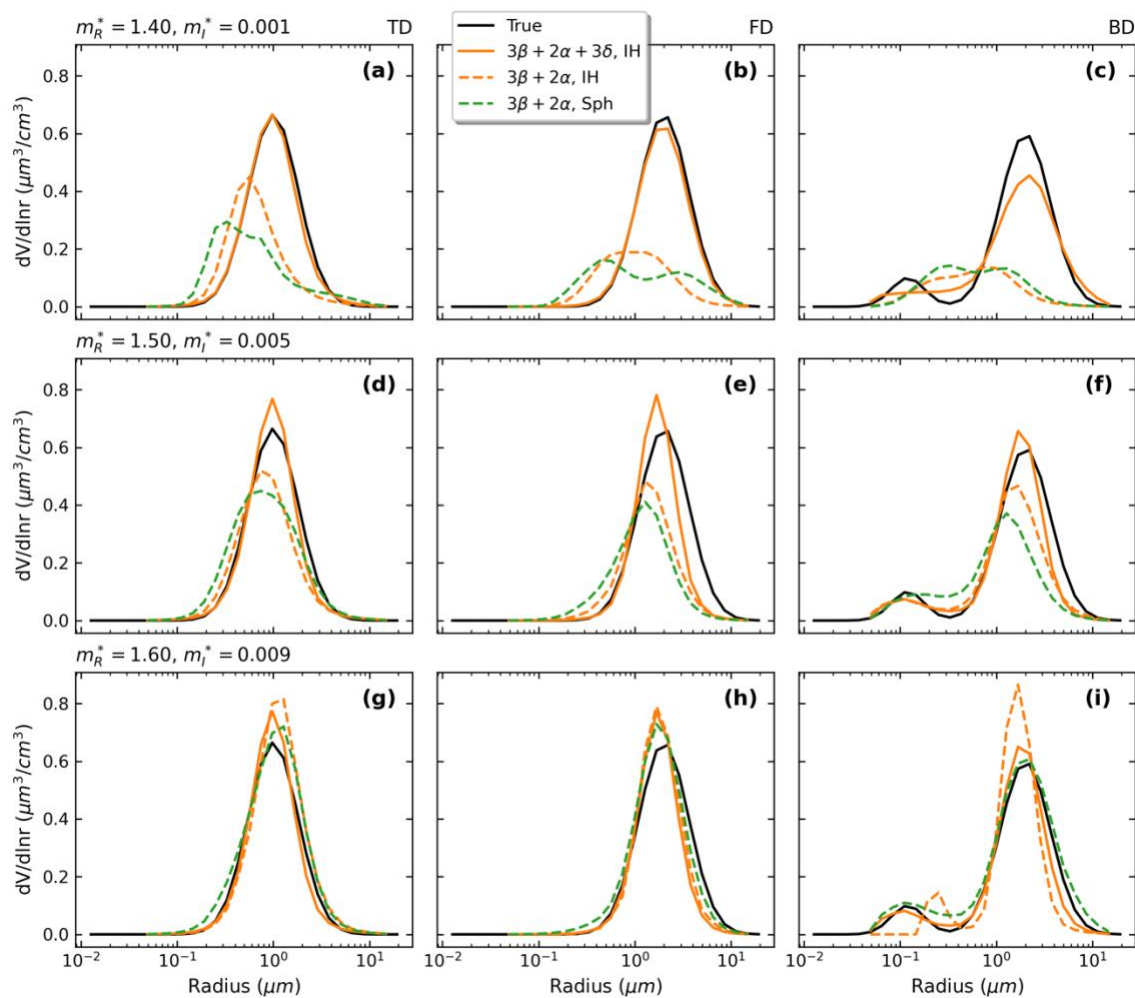
Figure 12. VSDs retrieved for the VSD types (columns) and three true CRI states (rows) from error-free synthetic measurements generated with the IH model. Like Fig. 11, different retrieval configurations are used.

4.3. Retrieval differences between the Spheroid and IH models

Figure 13 compares retrieval errors of V_t, r_{eff}, m_R, m_I when $(3\beta + 2\alpha)$ (top) and $(3\beta + 2\alpha + 3\delta)$ (bottom) are inverted with the IH (blue) and Spheroid (orange) models, respectively. Figure 14 is similar to Fig. 13 but illustrates retrieval errors of spectral SSA as well as fitting errors. The optical data are generated by the IH model from the TD type without considering measurement noise. The retrieval differences between the Spheroid and IH models are highlighted by the shaded areas. Note that the retrieval errors for the IH model are exactly the same as those shown in Fig. 11(a), (d), (g), (j), and keep in mind that the essential reason for the retrieval differences in this case is that the Spheroid model tries to fit the optical data generated by the IH model. Accordingly, retrieval differences are more significant for the inversion of $(3\beta + 2\alpha + 3\delta)$ than $(3\beta + 2\alpha)$ because PLDRs produced by the two non-spherical models show more prominent contrast than extinction or backscattering coefficient.

With regards to the $(3\beta + 2\alpha + 3\delta)$ inversion, the variation of the retrieval difference, as well as of the retrieval error, shows a clear positive correlation for V_t and r_{eff}, and for m_R and m_I, while it shows a negative correlation for V_t and m_R. It should be

505 noted that the largest retrieval difference occurs for $m_R^* = 1.6$, $m_I^* = 0.009$. This is because the m_R retrieved with the Spheroid model should keep a low value to fit the PLDR produced by the IH model, while the other retrieved parameters follow the aforementioned correlation relationships. As for the retrieval difference in SSA, it exhibits the same variation as the retrieval difference in m_I, except for that at 1064 nm, where the imaginary part is known as 0.001. Moreover, the error of fitting $(3\beta + 2\alpha + 3\delta)$ data for the Spheroid model shown in Fig. 14 (h) increases with the increase of m_R^* and decrease of m_I^*,

510 which corresponds to increasing IH-produced PLDR values that are harder for the Spheroid model to fit.
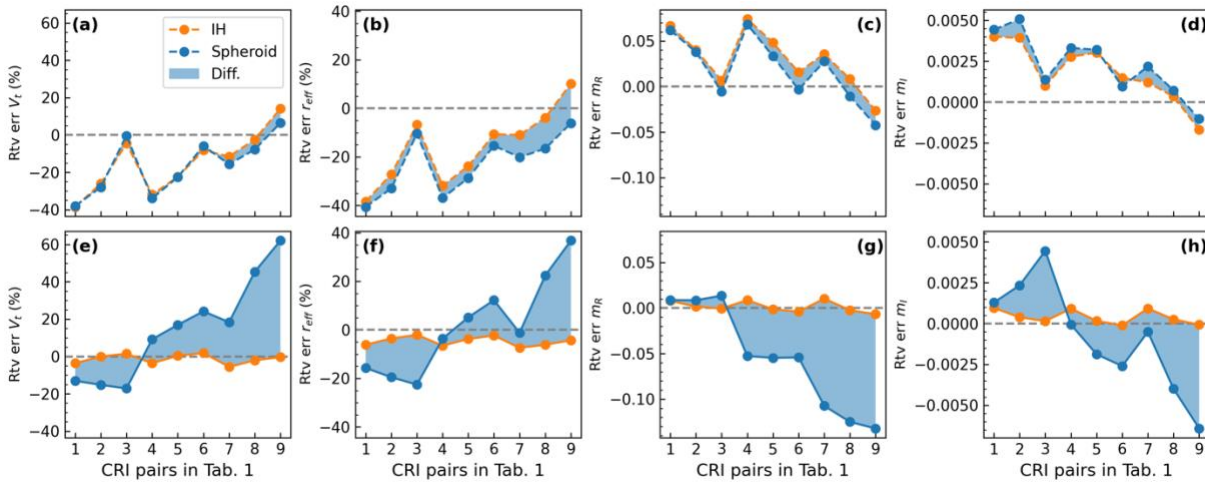
Figure 13. Retrieval errors of V_t, r_{eff}, m_R, m_I derived by inverting $(3\beta + 2\alpha)$ data (a–d, dashed lines) and $(3\beta + 2\alpha + 3\delta)$ data (e–h, solid lines) using the IH and Spheroid models, respectively. Differences between the IH and Spheroid models are indicated by shading. The optical data are generated from the TD type using the IH model without measurement noise.
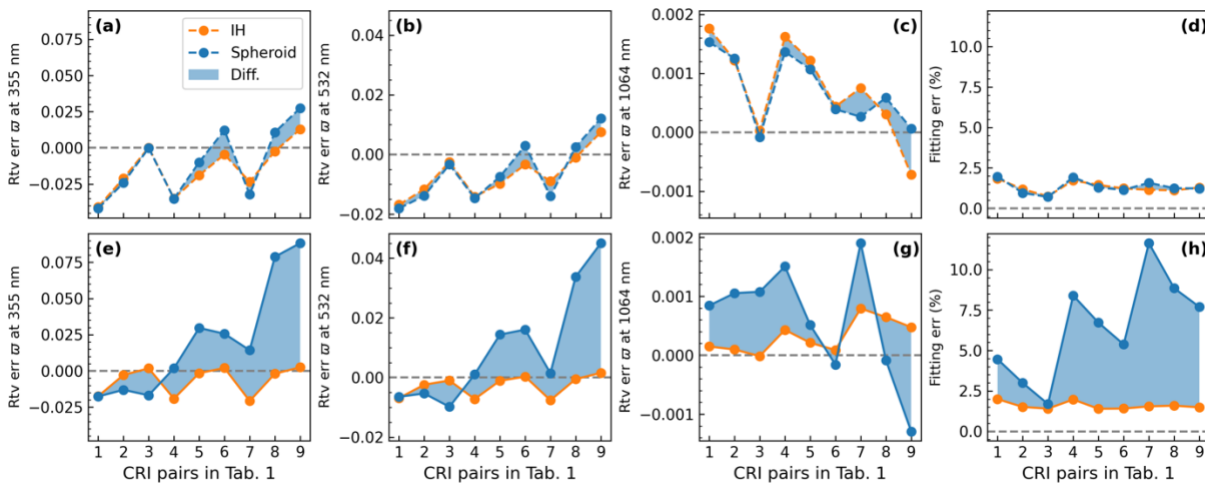
515 **Figure 14.** The same plot as Fig. 13 but for retrieval errors of spectral SSA (a–c and e–g) and errors of measurement fitting (d, h).

When the synthetic optical data are generated by the Spheroid model, the retrieval differences for $(3\beta + 2\alpha)$ inversion behave similarly to the counterparts shown in Figs. 14 and 15, while the differences for $(3\beta + 2\alpha + 3\delta)$ inversion show patterns distinct from Figs. 14 and 15 (see Figs. S2 and S3 in the Supplement). It is no wonder given the quite different PLDRs produced by

520 the two models at $r_{\mathrm{eff}} = 1\mu m$. However, when inverting the $(3\beta + 2\alpha + 3\delta)$ data, common features of the retrieval difference for the two scenarios turns out that: (1) compared to the IH model, the Spheroid model tends to derive smaller m_{R}; (2) as indicated in Table 2, if the Spheroid model derives a significantly smaller m_{R} (by more than 0.05) than the IH model (corresponding to $m_{\mathrm{R}}^* > 1.4$ in Table 2), it will also derive a smaller m_{I}, a larger V_{t} and a larger r_{eff}; whereas if the m_{R} retrieved with the Spheroid model is close to or even a little larger than that retrieved with the IH model (corresponding to

525 $m_{\mathrm{R}}^* = 1.4$ in Table 2), the Spheroid-retrieved m_{I} will be larger and V_{t}, r_{eff} smaller than the IH-retrieved counterparts.

Table 2. Average differences between the retrievals derived with the Spheroid and IH models for inversion of error-free synthetic data generated from the TD type with the IH models.

Inverted measurements	$m_{\mathrm{R}}^* = 1.4$				$m_{\mathrm{R}}^* > 1.4$			
	$\delta V_{\mathrm{t}}(\%)$	$\delta r_{\mathrm{eff}}(\%)$	$\delta m_{\mathrm{R}} \times 10^{-2}$	$\delta m_{\mathrm{I}} \times 10^{-3}$	$\delta V_{\mathrm{t}}(\%)$	$\delta r_{\mathrm{eff}}(\%)$	$\delta m_{\mathrm{R}} \times 10^{-2}$	$\delta m_{\mathrm{I}} \times 10^{-3}$
$3\beta + 2\alpha$	1	−4	−0.6	0.7	−3	−9	−1.4	0.4
$3\beta + 2\alpha + 3\delta$	−14	−15	0.7	2.2	31	17	−8.8	−2.9

4.4 Influence of measurement noise

We assume the measurement noise of each optical property is independent Gaussian noise. As demonstrated by Hu et al.

530 (2019), the maximum relative measurement errors are 10% for α_{355}, α_{532}, β_{355}, β_{532}; 15% for δ_{355}, δ_{532}, δ_{1064}; and 20% for β_{1064}. Therefore, the corresponding standard deviation of the noise distribution is a third of the maximum error. To investigate the influence of measurement noise, we repeat the retrieval processes in Sect. 4.2 but this time with the optical data perturbed by the assumed Gaussian noise. Figure 15 shows the distributions of the retrieval and fitting errors derived from the configurations: $(3\beta + 2\alpha + 3\delta,$ IH), $(3\beta + 2\alpha,$ IH), and $(3\beta + 2\alpha,$ Sphere) for inversions of 100 error-perturbed optical datasets.

535 Consistent with the error-free results, the retrieval from the full measurement set, specifically $(3\beta + 2\alpha + 3\delta)$, achieves the best accuracy in all cases, in terms of both dispersion and deviation from zero error. When inverting the $(3\beta + 2\alpha)$ data, regardless of the scattering model used, larger dispersion in the retrieval results is observed; in addition, the underestimation of both V_{t} and r_{eff} by the both models, the overestimation of m_{R} by the IH model, and the severe underestimation of m_{R} by the Sphere model are all in line with the results retrieved from the error-free optical data. Furthermore, note that the long tail of positive

540 $\varepsilon(\varpi)_{\mathrm{RMS}}$ occurring for the Sphere model corresponds to the long tail of positive $\varepsilon(m_{\mathrm{I}})$.
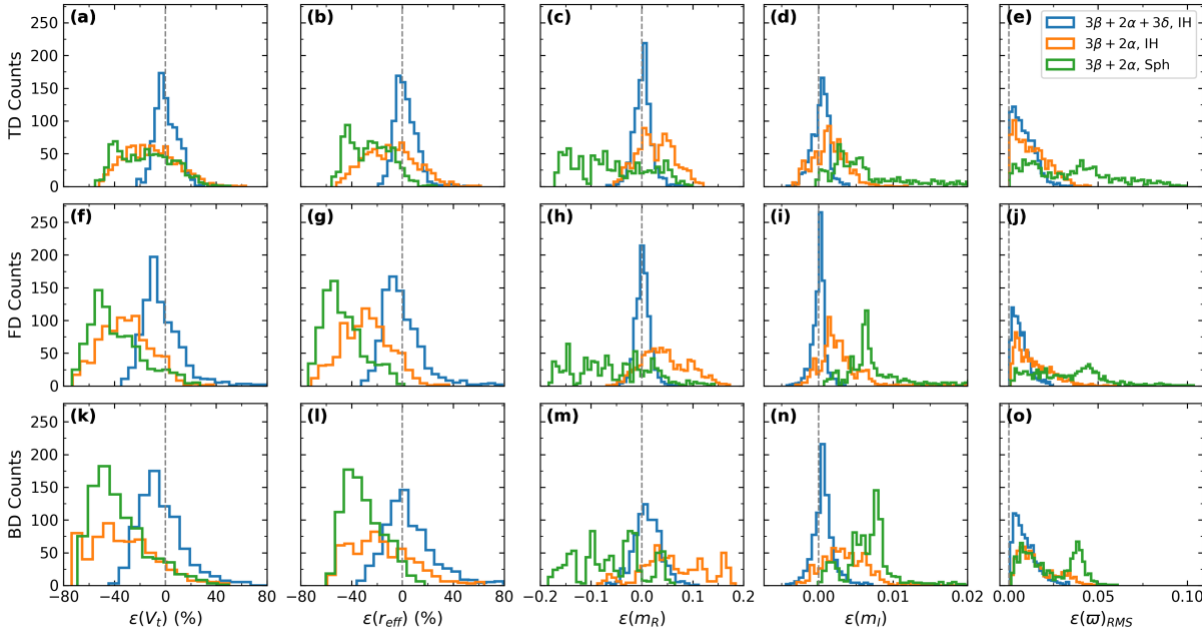
Figure 15. Distributions of retrieval errors of V_t, r_{eff}, m_R, m_I and ϖ derived by inverting error-perturbed synthetic optical data that are generated with the IH model. Different retrieval configurations: inversion of ($3\beta + 2\alpha + 3\delta$) with IH, inversion ($3\beta + 2\alpha$) with IH, inversion ($3\beta + 2\alpha$) with Sphere are used. Note that for easy-reading, the colour scheme is different from that in Fig. 11. From top to bottom rows, the panels correspond to the retrievals for the (a–e) TD, (f–j) FD, (k–o) BD types, respectively.

The means and standard deviations of the retrieval errors and fitting errors, calculated for different retrieval configurations and VSD types for both error-free and error-perturbed optical data, are listed in Tables 3 and 4 respectively. In both scenarios, retrieval errors have comparable mean values, but evidently larger standard deviations when measurement noise is present. Among the three retrieval configurations, the ($3\beta + 2\alpha + 3\delta$, IH) is the most adversely affected by measurement noise, but still achieves the best accuracy compared to the other configurations. Furthermore, the ε_{fit} for the (3+2+3, IH) configuration is the largest for both error-free and error-perturbed optical data, but at the same time, smaller than the RMS of the measurement uncertainty (4.2% for $3\beta + 2\alpha$ and 4.6% for $3\beta + 2\alpha + 3\delta$) in all cases.

Table 3. Mean and standard deviation (Std) (in paratheses) of retrieval errors and fitting errors for different VSD types derived by inverting the error-free synthetic optical data that are generated with the IH model. Different retrieval configurations are used.

VSD type		TD			FD			BD		
Rtv. config.		3+2+3, IH	3+2, IH	3+2, Sphere	3+2+3, IH	3+2, IH	3+2, Sphere	3+2+3, IH	3+2, IH	3+2, Sphere
$\varepsilon(V_t)(\%)$	Mean	−2	−14	−15	−10	−31	−37	−8	−27	−33
	Std	2	15	20	4	16	19	6	23	23
$\varepsilon(r_{eff})(\%)$	Mean	−1	−11	−25	−8	−28	−45	−2	4	−28
	Std	2	15	15	4	16	14	4	37	12

$\varepsilon(m_R)$	Mean	0.2	2.8	−5.9	0.1	4.3	−6.3	0.7	3.3	−6.7
$\times 10^{-2}$	Std	0.6	3.0	7.5	0.5	4.1	7	1.1	6.9	6.2
$\varepsilon(m_I)$	Mean	0.4	1.6	9.9	0.3	2.4	9.1	0.7	1.6	5.8
$\times 10^{-3}$	Std	0.4	1.7	8.9	0.2	1.8	6.5	0.2	3.1	2.3
$\varepsilon(\varpi)$	Mean	0.5	1.1	3.4	0.5	1.0	2.9	0.6	1.5	1.9
$\times 10^{-2}$	Std	0.4	0.8	2.4	0.1	0.7	1.7	0.4	0.9	1.3
$\varepsilon_{fit}(\%)$	Mean	1.5	1.2	1.3	1.3	1.4	0.8	1.7	3.3	0.7
	Std	0.2	0.3	0.5	0.1	0.6	0.3	0.3	3.1	0.2

555 **Table 4. Same as Table 5, but with error-perturbed synthetic optical data.**

		TD			FD			BD		
Retrieval error		3+2+3, IH	3+2, IH	3+2, Sphere	3+2+3, IH	3+2, IH	3+2, Sphere	3+2+3, IH	3+2, IH	3+2, Sphere
$\varepsilon(V_t)(\%)$	Mean	1	−12	−16	−3	−31	−39	−3	−34	−36
	Std	9	20	21	16	19	21	19	25	22
$\varepsilon(r_{eff})(\%)$	Mean	3	−9	−26	−0.4	−28	−46	6	−17	−30
	Std	9	20	16	16	19	16	21	24	15
$\varepsilon(m_R)$	Mean	0.2	2.7	−6.1	0.2	4.6	−5.8	1.1	6.3	−6.1
$\times 10^{-2}$	Std	1.7	3.6	7.2	1.4	4.6	7.4	2.5	6.3	6.3
$\varepsilon(m_I)$	Mean	0.2	1.5	9.2	0.0	3.0	10.1	0.6	3.6	7.0
$\times 10^{-3}$	Std	1.1	2.2	8.5	0.9	3.8	8.4	1.4	3.0	4.0
$\varepsilon(\varpi)$	Mean	0.8	1.3	3.4	0.7	1.3	3.3	0.9	1.6	2.3
$\times 10^{-2}$	Std	0.6	0.9	2.3	0.5	1.0	2.0	0.6	1.0	1.4
$\varepsilon_{fit}(\%)$	Mean	3.1	1.9	1.6	3.1	2.1	1.2	2.8	1.8	0.9
	Std	1.0	0.8	0.8	1.0	1.0	0.6	1.0	1.7	0.3

4.5 Conclusions drawn from the retrieval simulation

The comparison of simulated dust intensive optical properties with previous lidar measurements shows that qualities of the reproduced LR and PLDR for the Sphere, Spheroid and IH models differ as the utilized VSD changes. The discrepancies in EAE and BAE between the calculations and measurements indicate either the potential limitations of the scattering models to
560 reproduce the real measurements or the biases in the assumption of aerosol models.

Significant improvement of retrieval accuracy after incorporating 3δ into the inversion dataset is found, even if under the presence of measurement noise, while the inversion of conventional ($3\beta + 2\alpha$) data tends to underestimate V_t and r_{eff}. Furthermore, use of the Sphere model in non-spherical particle retrieval additionally leads to severe underestimation of m_R or

overestimation of m_I because this model generates stronger β. The simulation also shows that retrieval accuracy diminishes

565 with the increase of r_{eff}, decrease of CRI, and the presence of the fine mode. Due to the fact that Spheroid and IH models behave similarly in producing α and β, there is no significant difference between the retrievals by the two models with regard to the $(3\beta + 2\alpha)$ inversion. Nevertheless, more contrast emerges after the incorporation of 3δ measurements. The extent of the contrast depends on the exact state parameters of the particle ensemble.

5 BOREAL applications to real dust observations

570 In this section, we apply BOREAL algorithm to real lidar measurements obtained during two dust episodes to evaluate its performance under different configurations, specifically using different scattering models (Sphere, Spheroid or IH model) and input datasets. We only focus on pure dust observations which can be identified by analysing depolarization and fluorescence measurements of LILAS (Veselovskii et al., 2022).

5.1 Case 1: Fresh dust on 14 April 2019, Kashi

575 The first case is from the Dust Aerosol Observation (DAO) campaign where intensive field measurements were taken by LILAS and sun–sky photometers to study the mineral dust aerosol freshly emitted from the Taklamakan desert – one of the main sources of dust in Asia (Hu et al., 2020). On 15 April 2019, a dust activity was detected by LILAS at Kashi (39.50° N, 75.93° E) located on the western edge of the Taklamakan desert. Back trajectory analysis and satellite observations revealed it originated from the Taklamakan desert 1 or 2 days ago (Hu et al., 2020). Figure 16 is the range-corrected backscattered

580 signals at 1064 nm since 15 April 2019, 12:00 UTC. A continuous aerosol layer extending from the boundary layer (BL) to around 3.5 km is notable. Furthermore, clouds were continuously present during the period. Figure 17 displays the time-averaged optical profiles between 18:00 and 20:00 UTC, 15 April. The profiles indicate the particles were evenly distributed below 2.2 km with LR and PLDR values typical for pure dust.
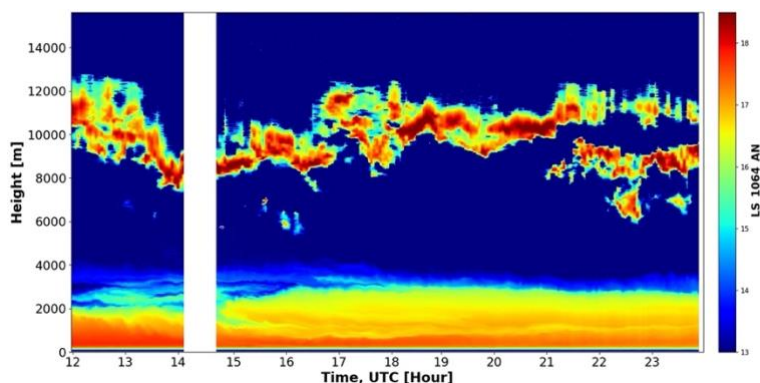
585 **Figure 16. LILAS range-corrected backscattered signals at 1064 nm between 15 April 2019, 12:00 UTC and 16 April 2019, 05:00 UTC, at Kashi, China.**
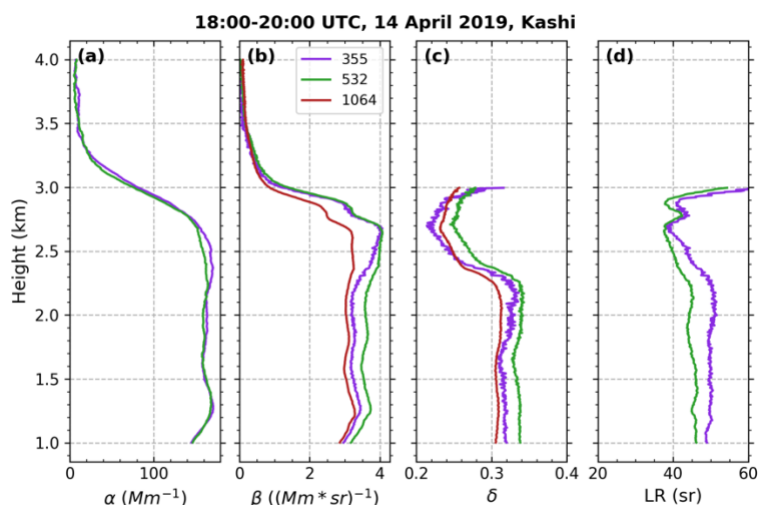
Figure 17. Optical profiles at 355, 532, and 1064 nm, averaged for the period 15 April 2019, 18:00–20:00 UTC, at Kashi. This figure is adapted from Fig. 10 in Hu et al. (2020).

590   Figure 18 shows the profiles of V_t, r_{eff}, m_R and $m_{I.355}$ for Case 1 retrieved with different retrieval configurations. The profiles of microphysical properties are stable below 2.2 km and present more variability above 2.2 km. In particular, the decline of r_{eff} above 2.2 km, retrieved from $(3\beta + 2\alpha + 3\delta)$ measurements, supports the conclusion drawn by Hu et al. (2020) that a lifted fine-mode anthropogenic aerosol layer was above the well-mixed dust layer due to convection. Different heights and retrieval configurations result in ranges of 35–85 μm^3/cm^3 for V_t, 0.4–1.3 μm for r_{eff}, 1.45–1.68 for m_R and 0.0015–0.012 for $m_{I.355}$.
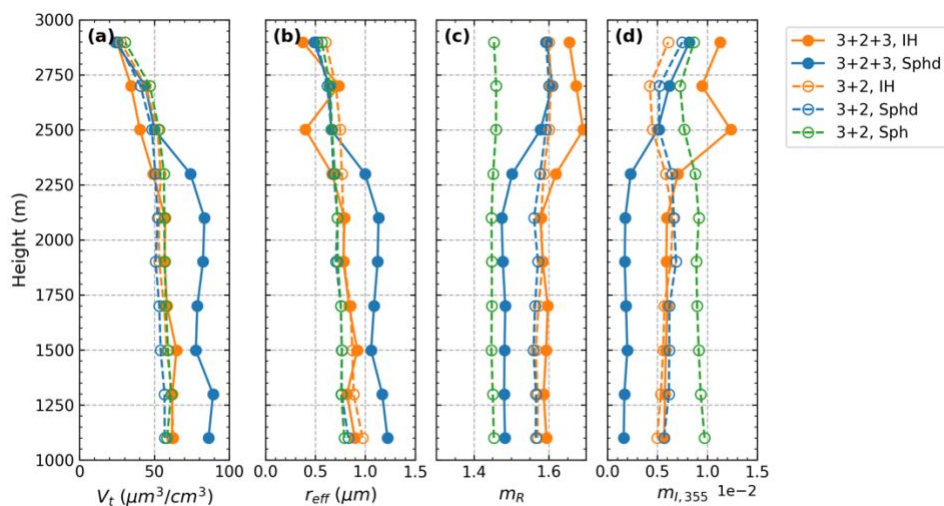
595

Figure 18. Profiles of (a) V_t, (b) r_{eff}, (c) m_R and (d) $m_{I.355}$ retrieved from the averaged optical data in Fig. 17 with different retrieval configurations: inversion of $(3\beta + 2\alpha + 3\delta)$ with the IH model (3+2+3, IH), inversion of $(3\beta + 2\alpha + 3\delta)$ with the Spheroid model (3+2+3, Sphd), inversion of $(3\beta + 2\alpha)$ with the IH model (3+2, IH), inversion of $(3\beta + 2\alpha)$ with the Spheroid model (3+2, Sphd) and inversion of $(3\beta + 2\alpha)$ with the Sphere (Sph) model (3+2, Sph).

600   Figure 19 displays more retrieval results for a layer averaged between 2 and 2.2 km, showing the VSD, m_R, spectral m_I and SSA, as well as the comparisons between the measured and recalculated optical properties (i.e., measurement fitting). All retrieval configurations derive monomodal VSD located in the coarse mode range, accompanied by m_R in 1.45–1.58, $m_{I,355}$ in 0.002–0.009, and ϖ_{355} in 0.87–0.94. The UV-enhanced imaginary part, and correspondingly, the UV-declined SSA are the consequences of considering the spectral dependence of dust aerosols. When the $(3\beta + 2\alpha)$ measurement are inverted, the 3

605   scattering models lead to similar V_t and r_{eff}; however, the Sphere model results in lower m_R and higher m_I. With the inclusion of 3δ measurements, V_t, r_{eff} increase while m_R, m_I decrease for both IH and Spheroid models; however, compared with the IH model, the Spheroid model derives higher V_t and r_{eff}, while lower m_R and m_I. Compared to the measurement error bars, all the scattering models are able to well fit the measurements. The AERONET level 2.0 retrieval at 15 April 2019, 3:50 UTC, Kashi, is also displayed for comparison. Compared to the BOREAL retrievals, the AERONET retrieval derives a coarse-mode-

610   predominating VSD with larger coarse-mode r_{eff} and a wavelength–independent m_R of ~1.54. Moreover, the spectral variations of m_I and SSA retrieved by AERONET are consistent with those retrieved by BOREAL.
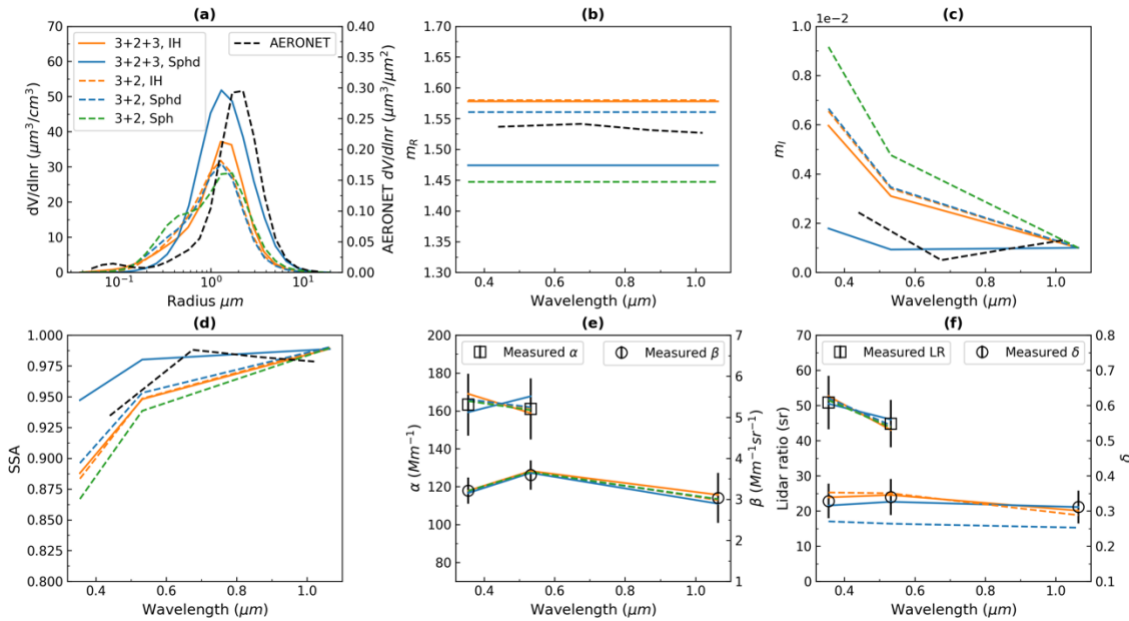
Figure 19. Retrievals and measurement fitting for the layer between 2 and 2.2 km in Case 1: (a) VSD, (b) m_R, (c) spectral m_I, (d) spectral SSA, (e) Fittings of α and β, (f) fittings of LRs and δ. Retrieval configurations are the same as those in Fig. 18. AERONET
615   **retrieval at 15 April 2019, 03:50 UTC are also shown in (a), (b), (c) and (d).**

5.2 Case 2: Transported dust on 21 March 2022, Lille

A dust plume above the boundary layer was observed by LILAS operated at the ATOLL on 21 March, 2022. The range-corrected signals and time-averaged optical profiles between 20:00 and 23:00 UTC are shown in Figs. 20 and 21. A separated aerosol layer between 5.4 and 5.6 km with δ_{355} around 0.3 can be distinguished. Figure 22 illustrates the 7-day back trajectory

620   of the layer starting at March 22, 00:00 UTC and the UV aerosol index (UVAI) on 17 March provided by the OMPS (ozone

mapping and profiler suite) instrument onboard Suomi–NPP satellite (Jaross, 2017). It indicates the air mass was originated from the Saharan region seven days ago and circled around in western Europe where a dust plume characterized by enhanced UVAI was observed by OMPS. Compared to the fresh dust observed in Case 1, the air mass underwent longer transport time.
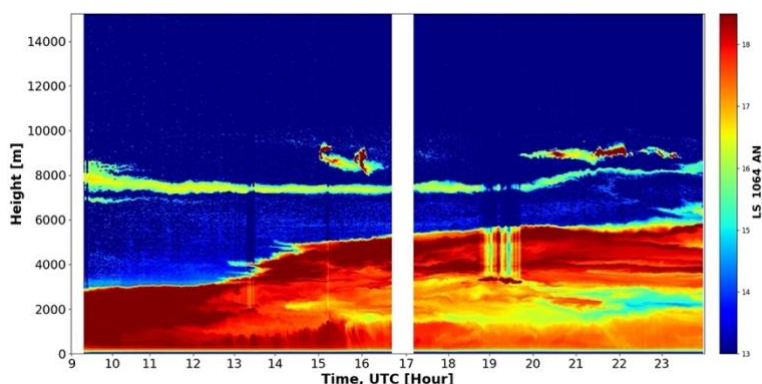
625 **Figure 20. LILAS range-corrected backscattered signals at 1064 nm since 21 March 2022, 9:00 UTC, at ATOLL/Lille, France.**
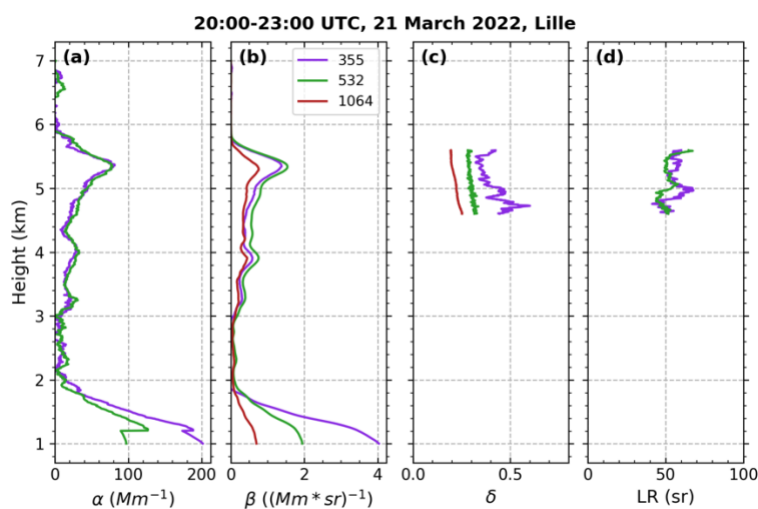
Figure 21. Same as Fig. 14 but for Case 2, averaged for the period 21 March 2022, 20:00–23:00 UTC, at ATOLL/Lille.
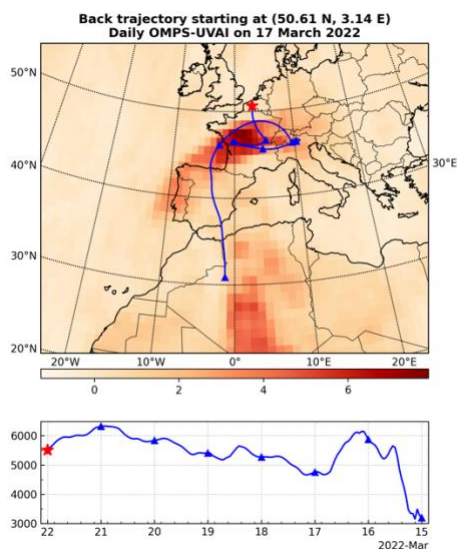
Figure 22. 7-day backward trajectory starting on 22 March 2022 at 5.3 km represented by the blue curve, over ATOLL/Lille (start marker), together with the UVAI measured by OMPS on 17 May 2023.

Figure 23 shows the retrievals of VSD, m_R, spectral m_I and SSA, as well as measurement fitting for the layer 5.4–5.6 km. All retrieval configurations derive monomodal VSDs with r_{eff} in 0.46–0.56 μm, accompanied by m_R in 1.45–1.64, $m_{I,355}$ in 0.0085–0.0175, and ϖ_{355} in 0.84–0.9. Compared to Case 1, the smaller r_{eff} in Case 2 is in line with the size evolution of dust particles during the transport processes (Arimoto et al., 1997; Hu, 2018; Uematsu et al., 1983). Furthermore, the overall higher m_I in Case 2 is consistent with laboratory measurements by Di Biagio et al. (2019) which manifests that Saharan dust is more absorbing than Taklamakan dust. Retrievals with all the scattering models effectively fit the measured optical properties within the measurement uncertainty. However, the IH model failed to accurately represent the spectral dependence of extinction coefficients measured by lidar. The AERONET level 1.5 retrieval at 21 March 2022, 15:58 UTC, Lille, is also shown for comparison. Note that it is the low aerosol loading ($AOD_{440} < 0.4$) that precludes the retrieval from being level 2.0. In other words, other metrices like solar zenith angle and sky error satisfy the level 2.0 criteria so that the retrieved CRI and absorption properties are still reliable (Holben et al., 2006). Unlike in Case 1, AERONET derives a bimodal VSD with the coarse-mode r_{eff} obviously larger than the BOREAL results. Moreover, compared to the BOREAL retrievals, the CRI from the AERONET retrieval is smaller and spectrally dependent for both real and imaginary parts. Compared to Case 1, the lidar profiles (Fig. 21) in Case 2 indicate more heterogeneity of aerosol vertical distribution and less contribution of the dust layer to the columnar optical properties which make the two types of retrieval less comparable.
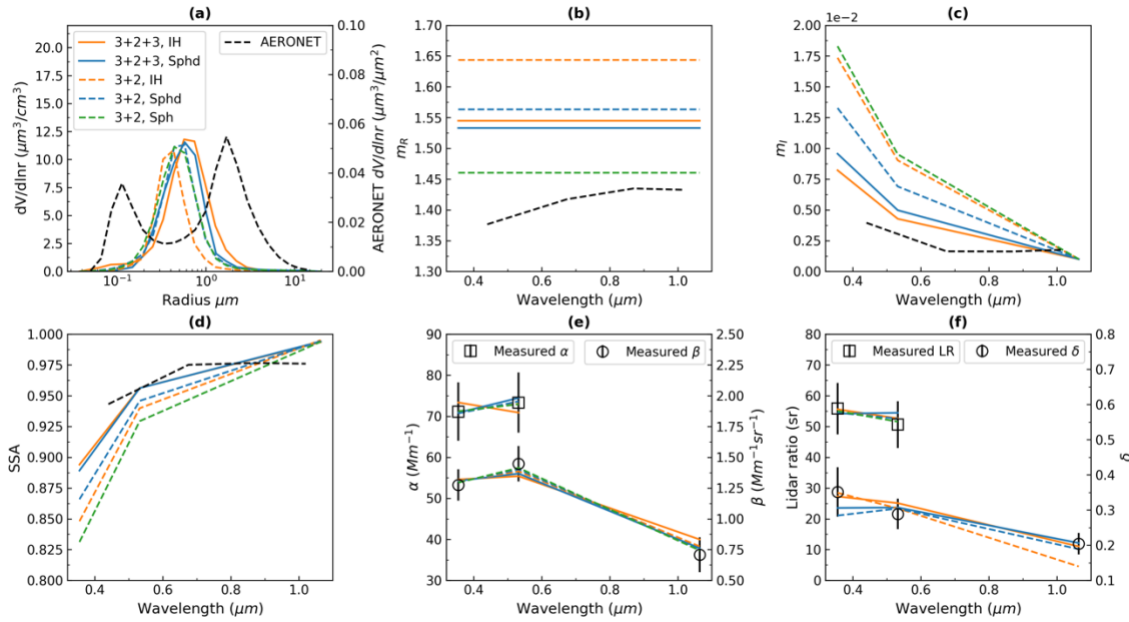
Figure 23. Same as Fig. 19 but for the layer 5.4–5.6 km in Case 2 and AERONET retrieval at 21 March 2022, 15:58 UTC.

Table 5 lists the detailed conditions of the two cases. Note the more intensive dust activity reflected in the layer thickness and the layer-averaged extinction coefficient in Case 1. Furthermore, the higher EAE provided by AERONET in Case 2 implies a

650   higher volume fraction of fine-mode particles. Table 6 summarizes the retrieved state parameters and measurement fittings in Figs. 19 and 23, together with the corresponding AERONET retrievals. The V_t in terms of AERONET is the layer-averaged volume concentration (the columnar volume concentration divided by the aerosol layer height estimated from the lidar profile), and the ε_{fit} in terms of AERONET refers to the sky error (the fitting of sky radiance measurements). Combining Table 6 and Figs. 19 and 23, when inverting ($3\beta + 2\alpha + 3\delta$) data, differences between the state parameters retrieved with the Spheroid

655   model and the IH model are more prominent in Case 1 than Case 2. All retrieval configurations lead to a ε_{fit} comparable to the root-mean-square uncertainty of the inverted measurements (4% for the ($3\beta + 2\alpha$) data and 4.4% for the ($3\beta + 2\alpha + 3\delta$) data). Compared to Case 1, the overall larger fitting error encountered in Case 2 might be attributed to the higher noise level because of the lower aerosol loading. The volume concentrations derived with BOREAL and AERONET are in the same order, while the effective radii derived with BOREAL are smaller than the corresponding AERONET values by 30–50% regardless of the

660   selection of the retrieval configuration.

Table 5. Detailed information about the dust cases.

		Case 1	Case 2
Meteorology	Date	15 April 2019	21 March 2022
	Site	Kashi (39.50N, 75.93E)	Lille (50.61N, 3.14E)
	Dust age	Fresh (<2 days)	Transported (~7 days)

Lidar	Time period (UTC)	18:00–20:00	20:00–23:00
	Dust layer (km)	1–2.2	5.4–5.6
	Layer–averaged α_{532} (Mm^{-1})	161	64
AERONET	Time (UTC)	03:50, 15 April 2019	15:58, 21 March 2022
	Retrieval level	L2	L1.5
	Col. AOD$_{440}$	0.65	0.28
	EAE$_{440-870}$	0.13	0.8

Table 6. State parameters for the selected layers in Case 1 and Case 2 retrieved by BOREAL and comparison with AERONET.

	State parameter	$3\beta + 2\alpha$			$3\beta + 2\alpha + 3\delta$		AERONET
		Sphere	Spheroid	IH	Spheroid	IH	
Case 1	r_{eff}(μm)	0.72	0.71	0.78	1.12	0.8	1.68[a]
	V_{t}(μm³/cm³)	57	51	53	83	58	129[b]
	m_{R}	1.45	1.56	1.58	1.47	1.58	1.53[c]
	m_{I}[c]	0.005	0.004	0.004	0.001	0.003	0.001
	ϖ[c]	0.932	0.947	0.941	0.972	0.942	0.971
	ε_{fit}(%)	1.2	1.4	1.6	3.2	2.6	5.19[d]
Case 2	r_{eff}(μm)	0.46	0.48	0.47	0.54	0.55	1.45[a]
	V_{t}(μm³/cm³)	13	12	11	14	14	15[b]
	m_{R}	1.46	1.56	1.64	1.53	1.55	1.42[c]
	m_{I}[c]	0.010	0.007	0.009	0.005	0.004	0.002
	ϖ[c]	0.918	0.935	0.928	0.947	0.948	0.968
	ε_{fit}(%)	3.1	3.4	5.6	6.5	7.9	2.16[d]

[a] AERONET coarse–mode effective radius; [b] layer–averaged volume concentration; [c] spectrally averaged value; [d] error of fitting sky radiance measurements.

6 Discussion

The retrievals from both synthetic optical data (Sect. 4) and real lidar observations (Sect. 5) show results that fit the measurements within the prescribed measurement uncertainty, regardless of the retrieval configurations, i.e., different choices of scattering model and input measurements. This indicates that BOREAL combining with any of the scattering model is able to retrieve state parameters that well reproduce the input measurements. However, with regards to different retrieval configurations, the retrievals differ to various extent.

When the conventional ($3\beta + 2\alpha$) data are inverted, all three scattering models behave similarly for particle size retrieval, resulting in similar VSD, V_{t} and r_{eff}. Moreover, due to the limited sensitivity of ($3\beta + 2\alpha$) to large particles, the retrieved V_{t}

and r_{eff} tend to be underestimated, accompanied by m_{R} and m_{I} that are often overestimated. Such retrieval bias exacerbates with the increase of particle size. However, using the Sphere model to retrieve non-spherical particles results in severe

675 underestimation of m_{R} or overestimation of m_{I} so as to compensate for the strongly enhanced backscattering coefficient caused by the spherical particle assumption.

When the augmented ($3\beta + 2\alpha + 3\delta$) data are inverted, apparent improvement of retrieval accuracy for use of non-spherical models is observed due to the extended information contents provided by the additional spectral PLDR measurements. Nevertheless, the extent of the improvement depends on the model's representation of PLDR. The simulations have shown

680 that the model-produced PLDR exhibits various sensitivities to the state parameters when they change, which means the scattering model has different information contents for different domains of the state parameters. Tables 3 and 4 indicate the larger the particle size, the higher the retrieval bias for the ($3\beta + 2\alpha$) inversion, and the more improvement after the inclusion of 3δ.

Retrieval difference between the two non-spherical models stems from their difference in representing lidar-measured optical

685 properties, of which the extent in turn depends on the retrieved state parameters. This can be further illustrated by looking at the two real case retrievals in Sect. 5. In Case 1 (fresh Taklamakan dust), when inverting ($3\beta + 2\alpha$), the r_{eff} is retrieved similarly by the two non-spherical models between 0.71–0.78 μm, a range where the ($3\beta + 2\alpha$) data yielded by the two non-spherical models show little difference. As a result, other state parameters are also retrieved similarly by the two non-spherical models. When inverting ($3\beta + 2\alpha + 3\delta$), however, obvious retrieval difference in Case 1 is observed –compared to the IH model, the

690 Spheroid model derives higher V_{t} and r_{eff} while lower m_{R} and m_{I} (consistent with the results shown in Fig. 13) because of significant contrast between the PLDR produced by the two non-spherical models. To the contrary, in Case 2 (transported Saharan dust), when inverting ($3\beta + 2\alpha + 3\delta$), the r_{eff} is retrieved by the two non-spherical models between 0.54–0.55 μm, a region where the ($3\beta + 2\alpha + 3\delta$) data yielded by the two non-spherical models do not exhibit clear contrasts and consequently, other state parameters are also retrieved similarly by the two non-spherical models. With an absence of 3δ, as demonstrated

695 above, the r_{eff} decreases to 11–12 μm due to the loss of sensitivity. However, compared to the IH model, the Spheroid model retrieves lower m_{I} and significantly lower m_{R} as a response of the β difference between the two non-spherical models which approaches to the maximum in the retrieved r_{eff} range (Fig. 4).

The comparison between BOREAL and AERONET retrievals on the one hand substantiates the significance of considering dust non-sphericity and incorporating the spectral PLDR measurements to improve the retrieval accuracy. On the other hand,

700 it manifests the limitations of both IH and Spheroid models in reproducing the PLDR measurement. For example, in Case 1, the value of r_{eff} indeed increases after incorporating 3δ into the inversion dataset. However, neither the IH nor Spheroid model can derive a r_{eff} close to the AERONET-retrieved value in order to fit the spectral PLDR lidar measurements. Consequently, the robustness of the retrieval results and the consistency between simulations and real dust retrievals are encouraging; meanwhile, we should be aware of the limitations of the non-spherical models in reproducing lidar-backward measurements

705 and its influence on the dust retrieval.

7 Conclusions

In this study, we investigate the feasibility of retrieving microphysical properties (state parameters) of dust aerosols, including the VSD, volume concentration (V_t), effective radius (r_{eff}), CRI, and SSA (ϖ) from combinations of spectral extinction (α), backscattering (β) and PLDR (δ) lidar measurements. For the first time, optical properties simulated with three scattering

710 models: the Sphere, Spheroid and IH models are compared and their sensitivities to the state parameters are assessed. Using the BOREAL retrieval algorithm, we evaluate the influence of utilizing the aforementioned scattering models to invert different lidar measurement sets on the retrieval results. The simulations reveal that in a typical dust size range, the Sphere model can overestimate the backscattering coefficient of non-spherical dust particles by a factor of 5 at most, which causes severe underestimation of the real part (m_R) of the CRI (by ~0.2 at most) and overestimation of the imaginary part (m_I) of the CRI

715 (by ~0.025 at most). Meanwhile, the simulations manifest great improvement of retrieval accuracy after incorporating the 3δ measurements into the conventional inversion of the $3\beta + 2\alpha$ measurements – with the presence of measurement noise, accuracies of 10–22% for V_t, 12%–27% for r_{eff}, 0.02–0.036 for m_R, 0.001–0.002 for m_I, and 0.012–0.015 for ϖ are achieved for defined aerosol models. However, compared to extinction and backscattering coefficients, obvious distinctions between the two non-spherical models (Spheroid and IH models) lie in the representation of PLDR, which results in an increase of

720 retrieval difference between the two non-spherical models after the inclusion of depolarization measurements. The extent of this retrieval difference depends on the retrieved r_{eff}.

The retrievals from real lidar measurements consolidate the results and substantiate the conclusions derived from the simulations. On the other hand, they expose some issues worth noting. When inverting ($3\beta + 2\alpha + 3\delta$) measurements, retrieval differences between the IH and Spheroid models for the fresh Taklamakan dust retrieval are 30% for V_t, 29% for r_{eff}, 0.11 for

725 m_R, 0.002 for spectral-averaged m_I, and 0.03 for spectral-averaged ϖ, respectively, larger than those for the transported Saharan dust retrieval. All the retrievals fit the measurements well with a fitting error comparable with the measurement uncertainty. The comparison with corresponding AERONET retrievals indicates that when inverting ($3\beta + 2\alpha + 3\delta$) measurements, the lidar-retrieved r_{eff} can be smaller by 30–50%. Apart from the reason that the difference in measurement time and vertical inhomogeneity of the aerosols make the two types of retrievals less comparable and the reason that BOREAL

730 has the trend to underestimate particle size due to the reduction of measurement sensitivity to large particles, it is also a result of fitting the depolarization measurements for the used non-spherical model. Among the exploited retrieval configurations, the ($3\beta + 2\alpha + 3\delta$, Spheroid) configuration derives the results most consistent with AERONET because the Spheroid model is also exploited by AERONET for dust retrievals.

This study demonstrates the robustness of the retrieval method (BOREAL) for retrieving dust microphysical properties from

735 combined spectral extinction, backscattering and depolarization lidar measurements. However, on the other hand, it reveals potential limitations of the IH and Spheroid models in producing dust backscattering properties, particularly the PLDR, which result in biases not only between the retrievals from the two non-spherical models, but also between the retrievals from lidars and other types of measurements (sun–sky photometers, in situ, laboratory measurements, etc.). Such biases will undoubtedly

increase the uncertainty in aerosol modelling and radiative effect estimation that further studies are needed to evaluate in the
740   future.

Data availability. The data are available upon request.

Author contributions. YC developed the retrieval algorithm, performed simulations and real data applications, and wrote the manuscript. QH provided lidar optical measurements and helped with data analysis and manuscript revision. PG is the PI of the project, supervised the study and improved the manuscript. IV helped in establishing the lidar system and scientific
745   arguments. AL, OD and CC provided the Sphere and Spheroid model and shared expertise in aerosol retrievals. MS developed and provided the IH model. FD helped with the programming. TP and GD took the charge of the maintenance, automatization and operation of the lidar system, and provided raw data processing.

Competing interests. The contact author has declared that neither the author nor co-authors have any competing interests.

Acknowledgements. We acknowledge the Labex CaPPA (Chemical and Physical Properties of the Atmosphere) for the
750   support of this research. We also thank Philippe Goloub (PI) for his effort in establishing and maintaining the Lille site and the Kashi site used in this investigation, NOAA Air Resources Laboratory (ARL) for sharing meteorology data and providing the HYSPLIT models.

Financial support. This research has been supported by the French National Research Agency (ANR) through the PIA (Programme d'Investissement d'Avenir) under contract "ANR-11-LABX-0005-01" and by the Hauts-de-France regional
755   council and the European Funds for Regional Economic Development (FEDER).

References

Alfaro, S. C., Gaudichet, A., Gomes, L., and Maillé, M.: Modeling the size distribution of a soil aerosol produced by sandblasting, J. Geophys. Res. Atmospheres, 102, 11239–11249, https://doi.org/10.1029/97JD00403, 1997.

d'Almeida, G. A. and Schütz, L.: Number, Mass and Volume Distributions of Mineral Aerosol and Soils of the Sahara, J.
760   Appl. Meteorol. Climatol., 22, 233–243, https://doi.org/10.1175/1520-0450(1983)022<0233:NMAVDO>2.0.CO;2, 1983.

Ansmann, A., Mamouri, R.-E., Bühl, J., Seifert, P., Engelmann, R., Hofer, J., Nisantzi, A., Atkinson, J. D., Kanji, Z. A., Sierau, B., Vrekoussis, M., and Sciare, J.: Ice-nucleating particle versus ice crystal number concentrationin altocumulus and cirrus layers embedded in Saharan dust:a closure study, Atmospheric Chem. Phys., 19, 15087–15115, https://doi.org/10.5194/acp-19-15087-2019, 2019.

765   Arimoto, R., Ray, B. J., Lewis, N. F., Tomza, U., and Duce, R. A.: Mass-particle size distributions of atmospheric dust and the dry deposition of dust to the remote ocean, J. Geophys. Res. Atmospheres, 102, 15867–15874, https://doi.org/10.1029/97JD00796, 1997.

Bangert, M., Nenes, A., Vogel, B., Vogel, H., Barahona, D., Karydis, V. A., Kumar, P., Kottmeier, C., and Blahak, U.: Saharan dust event impacts on cloud formation and radiation over Western Europe, Atmospheric Chem. Phys., 12, 4045–4063,
770   https://doi.org/10.5194/acp-12-4045-2012, 2012.

Bi, L., Yang, P., Kattawar, G. W., and Mishchenko, M. I.: Efficient implementation of the invariant imbedding T-matrix method and the separation of variables method applied to large nonspherical inhomogeneous particles, J. Quant. Spectrosc. Radiat. Transf., 116, 169–183, https://doi.org/10.1016/j.jqsrt.2012.11.014, 2013.

Bohren, C. F. and Huffman, D. R.: Absorption and scattering of light by small particles, Wiley-VCH, Weinheim, 530 pp., 2004.

Borovoi, A., Konoshonkin, A., and Kustova, N.: Backscattering reciprocity for large particles, Opt. Lett., 38, 1485–1487, https://doi.org/10.1364/OL.38.001485, 2013.

Burton, S. P., Ferrare, R. A., Hostetler, C. A., Hair, J. W., Rogers, R. R., Obland, M. D., Butler, C. F., Cook, A. L., Harper, D. B., and Froyd, K. D.: Aerosol classification using airborne High Spectral Resolution Lidar measurements – methodology and examples, Atmospheric Meas. Tech., 5, 73–98, https://doi.org/10.5194/amt-5-73-2012, 2012.

Burton, S. P., Chemyakin, E., Liu, X., Knobelspiesse, K., Stamnes, S., Sawamura, P., Moore, R. H., Hostetler, C. A., and Ferrare, R. A.: Information content and sensitivity of the 3$\beta +$\,2α lidar measurement system for aerosol microphysical retrievals, Atmospheric Meas. Tech., 9, 5555–5574, https://doi.org/10.5194/amt-9-5555-2016, 2016.

Chang, Y., Hu, Q., Goloub, P., Veselovskii, I., and Podvin, T.: Retrieval of Aerosol Microphysical Properties from Multi-Wavelength Mie–Raman Lidar Using Maximum Likelihood Estimation: Algorithm, Performance, and Application, Remote Sens., 14, 6208, https://doi.org/10.3390/rs14246208, 2022.

Chin, M., Ginoux, P., Kinne, S., Torres, O., Holben, B. N., Duncan, B. N., Martin, R. V., Logan, J. A., Higurashi, A., and Nakajima, T.: Tropospheric Aerosol Optical Thickness from the GOCART Model and Comparisons with Satellite and Sun Photometer Measurements, J. Atmospheric Sci., 59, 461–483, https://doi.org/10.1175/1520-0469(2002)059<0461:TAOTFT>2.0.CO;2, 2002.

DeMott, P. J., Sassen, K., Poellot, M. R., Baumgardner, D., Rogers, D. C., Brooks, S. D., Prenni, A. J., and Kreidenweis, S. M.: African dust aerosols as atmospheric ice nuclei, Geophys. Res. Lett., 30, https://doi.org/10.1029/2003GL017410, 2003.

Di Biagio, C., Formenti, P., Balkanski, Y., Caponi, L., Cazaunau, M., Pangui, E., Journet, E., Nowak, S., Andreae, M. O., Kandler, K., Saeed, T., Piketh, S., Seibert, D., Williams, E., and Doussin, J.-F.: Complex refractive indices and single-scattering albedo of global dust aerosols in the shortwave spectrum and relationship to size and iron content, Atmospheric Chem. Phys., 19, 15503–15531, https://doi.org/10.5194/acp-19-15503-2019, 2019.

Dubovik, O. and King, M. D.: A flexible inversion algorithm for retrieval of aerosol optical properties from Sun and sky radiance measurements, J. Geophys. Res. Atmospheres, 105, 20673–20696, https://doi.org/10.1029/2000JD900282, 2000.

Dubovik, O., Holben, B., Eck, T. F., Smirnov, A., Kaufman, Y. J., King, M. D., Tanré, D., and Slutsker, I.: Variability of Absorption and Optical Properties of Key Aerosol Types Observed in Worldwide Locations, J. Atmospheric Sci., 59, 590–608, https://doi.org/10.1175/1520-0469(2002)059<0590:VOAAOP>2.0.CO;2, 2002.

Dubovik, O., Sinyuk, A., Lapyonok, T., Holben, B. N., Mishchenko, M., Yang, P., Eck, T. F., Volten, H., Muñoz, O., Veihelmann, B., van der Zande, W. J., Leon, J.-F., Sorokin, M., and Slutsker, I.: Application of spheroid models to account for aerosol particle nonsphericity in remote sensing of desert dust, J. Geophys. Res. Atmospheres, 111, https://doi.org/10.1029/2005JD006619, 2006.

Floutsi, A. A., Baars, H., Engelmann, R., Althausen, D., Ansmann, A., Bohlmann, S., Heese, B., Hofer, J., Kanitz, T., Haarig, M., Ohneiser, K., Radenz, M., Seifert, P., Skupin, A., Yin, Z., Abdullaev, S. F., Komppula, M., Filioglou, M., Giannakaki, E., Stachlewska, I. S., Janicka, L., Bortoli, D., Marinou, E., Amiridis, V., Gialitaki, A., Mamouri, R.-E., Barja, B., and Wandinger,

U.: DeLiAn – a growing collection of depolarization ratio, lidar ratio and Ångström exponent for different aerosol types and mixtures from ground-based lidar observations, Atmospheric Meas. Tech., 16, 2353–2379, https://doi.org/10.5194/amt-16-2353-2023, 2023.

Giannadaki, D., Pozzer, A., and Lelieveld, J.: Modeled global effects of airborne desert dust on air quality and premature mortality, Atmospheric Chem. Phys., 14, 957–968, https://doi.org/10.5194/acp-14-957-2014, 2014.

Gomes, L., Bergametti, G., Coudé-Gaussen, G., and Rognon, P.: Submicron desert dusts: A sandblasting process, J. Geophys. Res. Atmospheres, 95, 13927–13935, https://doi.org/10.1029/JD095iD09p13927, 1990.

Haarig, M., Ansmann, A., Engelmann, R., Baars, H., Toledano, C., Torres, B., Althausen, D., Radenz, M., and Wandinger, U.: First triple-wavelength lidar observations of depolarization and extinction-to-backscatter ratios of Saharan dust, Atmospheric Chem. Phys., 22, 355–369, https://doi.org/10.5194/acp-22-355-2022, 2022.

Hansen, J. E. and Travis, L. D.: Light scattering in planetary atmospheres, Space Sci. Rev., 16, 527–610, https://doi.org/10.1007/BF00168069, 1974.

Hess, M., Koepke, P., and Schult, I.: Optical Properties of Aerosols and Clouds: The Software Package OPAC, Bull. Am. Meteorol. Soc., 79, 831–844, https://doi.org/10.1175/1520-0477(1998)079<0831:OPOAAC>2.0.CO;2, 1998.

Holben, B. N., Eck, T. F., Slutsker, I., Tanré, D., Buis, J. P., Setzer, A., Vermote, E., Reagan, J. A., Kaufman, Y. J., Nakajima, T., Lavenu, F., Jankowiak, I., and Smirnov, A.: AERONET—A Federated Instrument Network and Data Archive for Aerosol Characterization, Remote Sens. Environ., 66, 1–16, https://doi.org/10.1016/S0034-4257(98)00031-5, 1998.

Holben, B. N., Eck, T. F., Slutsker, I., Smirnov, A., Sinyuk, A., Schafer, J., Giles, D., and Dubovik, O.: Aeronet's Version 2.0 quality assurance criteria, in: Remote Sensing of the Atmosphere and Clouds, Remote Sensing of the Atmosphere and Clouds, 134–147, https://doi.org/10.1117/12.706524, 2006.

Hu, Q.: Advanced aerosol characterization using sun/sky photometer and multi-wavelength Mie-Raman lidar measurements, These de doctorat, Université de Lille (2018-2021), 2018.

Hu, Q., Goloub, P., Veselovskii, I., Bravo-Aranda, J.-A., Popovici, I. E., Podvin, T., Haeffelin, M., Lopatin, A., Dubovik, O., Pietras, C., Huang, X., Torres, B., and Chen, C.: Long-range-transported Canadian smoke plumes in the lower stratosphere over northern France, Atmospheric Chem. Phys., 19, 1173–1193, https://doi.org/10.5194/acp-19-1173-2019, 2019.

Hu, Q., Wang, H., Goloub, P., Li, Z., Veselovskii, I., Podvin, T., Li, K., and Korenskiy, M.: The characterization of Taklamakan dust properties using a multiwavelength Raman polarization lidar in Kashi, China, Atmospheric Chem. Phys., 20, 13817–13834, https://doi.org/10.5194/acp-20-13817-2020, 2020.

Huang, Y., Kok, J. F., Saito, M., and Muñoz, O.: Single-scattering properties of ellipsoidal dust aerosols constrained by measured dust shape distributions, Atmospheric Chem. Phys., 23, 2557–2577, https://doi.org/10.5194/acp-23-2557-2023, 2023.

van de Hulst, H. C.: Light Scattering by Small Particles., John Wiley and Sons, New York, 1957.

Johnson, B. R.: Invariant imbedding T matrix approach to electromagnetic scattering, Appl. Opt., 27, 4861–4873, https://doi.org/10.1364/AO.27.004861, 1988.

Kandler, K., Benker, N., Bundke, U., Cuevas, E., Ebert, M., Knippertz, P., Rodríguez, S., Schütz, L., and Weinbruch, S.:
Chemical composition and complex refractive index of Saharan Mineral Dust at Izaña, Tenerife (Spain) derived by electron
845   microscopy, Atmos. Environ., 41, 8058–8074, https://doi.org/10.1016/j.atmosenv.2007.06.047, 2007.

Kandler, K., Schütz, L., Deutscher, C., Ebert, M., Hofmann, H., Jäckel, S., Jaenicke, R., Knippertz, P., Lieke, K., Massling,
A., Petzold, A., Schladitz, A., Weinzierl, B., Wiedensohler, A., Zorn, S., and Weinbruch, S.: Size distribution, mass
concentration, chemical and mineralogical composition and derived optical parameters of the boundary layer aerosol at Tinfou,
Morocco, during SAMUM 2006, Tellus B Chem. Phys. Meteorol., 61, 32, https://doi.org/10.1111/j.1600-0889.2008.00385.x,
850   2009.

Kaufman, Y. J., Koren, I., Remer, L. A., Tanré, D., Ginoux, P., and Fan, S.: Dust transport and deposition observed from the
Terra-Moderate Resolution Imaging Spectroradiometer (MODIS) spacecraft over the Atlantic Ocean, J. Geophys. Res.
Atmospheres, 110, https://doi.org/10.1029/2003JD004436, 2005.

Kok, J. F. and Renno, N. O.: A comprehensive numerical model of steady state saltation (COMSALT), J. Geophys. Res.
855   Atmospheres, 114, https://doi.org/10.1029/2009JD011702, 2009.

Levy, R. C., Remer, L. A., Mattoo, S., Vermote, E. F., and Kaufman, Y. J.: Second-generation operational algorithm: Retrieval
of aerosol properties over land from inversion of Moderate Resolution Imaging Spectroradiometer spectral reflectance, J.
Geophys. Res. Atmospheres, 112, https://doi.org/10.1029/2006JD007811, 2007.

Maring, H., Savoie, D. L., Izaguirre, M. A., Custals, L., and Reid, J. S.: Mineral dust aerosol size distribution change during
860   atmospheric transport, J. Geophys. Res. Atmospheres, 108, https://doi.org/10.1029/2002JD002536, 2003.

Mayer, B. and Kylling, A.: Technical note: The libRadtran software package for radiative transfer calculations - description
and examples of use, Atmospheric Chem. Phys., 5, 1855–1877, https://doi.org/10.5194/acp-5-1855-2005, 2005.

Miller, R. L. and Tegen, I.: Climate Response to Soil Dust Aerosols, J. Clim., 11, 3247–3267, https://doi.org/10.1175/1520-
0442(1998)011<3247:CRTSDA>2.0.CO;2, 1998.

865   Miller, R. L., Tegen, I., and Perlwitz, J.: Surface radiative forcing by soil dust aerosols and the hydrologic cycle, J. Geophys.
Res. Atmospheres, 109, https://doi.org/10.1029/2003JD004085, 2004.

Mishchenko, M. I. and Travis, L. D.: T-matrix computations of light scattering by large spheroidal particles, Opt. Commun.,
109, 16–21, https://doi.org/10.1016/0030-4018(94)90731-5, 1994.

Mishchenko, M. I., Travis, L. D., and Lacis, A. A.: Scattering, Absorption, and Emission of Light by Small Particles,
870   Cambridge University Press, Cambridge, 2002.

Müller, D., Wandinger, U., and Ansmann, A.: Microphysical particle parameters from extinction and backscatter lidar data by
inversion with regularization: theory, Appl Opt, 38, 2346–2357, https://doi.org/10.1364/AO.38.002346, 1999.

Müller, D., Veselovskii, I., Kolgotin, A., Tesche, M., Ansmann, A., and Dubovik, O.: Vertical profiles of pure dust and mixed
smoke–dust plumes inferred from inversion of multiwavelength Raman/polarization lidar data and comparison to
875   AERONET retrievals and in situ observations, Appl Opt, 52, 3178–3202, https://doi.org/10.1364/AO.52.003178, 2013.

Nakajima, T., Tanaka, M., Yamano, M., Shiobara, M., Arao, K., and Nakanishi, Y.: Aerosol Optical Characteristics in the
Yellow Sand Events Observed in May, 1982 at Nagasaki-Part II Models, J. Meteorol. Soc. Jpn. Ser II, 67, 279–291,
https://doi.org/10.2151/jmsj1965.67.2_279, 1989.

880 Nicolae, D., Vasilescu, J., Talianu, C., Binietoglou, I., Nicolae, V., Andrei, S., and Antonescu, B.: A neural network aerosol-typing algorithm based on lidar data, Atmospheric Chem. Phys., 18, 14511–14537, https://doi.org/10.5194/acp-18-14511-2018, 2018.

Osborne, S. R., Johnson, B. T., Haywood, J. M., Baran, A. J., Harrison, M. a. J., and McConnell, C. L.: Physical and optical properties of mineral dust aerosol during the Dust and Biomass-burning Experiment, J. Geophys. Res. Atmospheres, 113, https://doi.org/10.1029/2007JD009551, 2008.

885 Reid, J. S., Jonsson, H. H., Maring, H. B., Smirnov, A., Savoie, D. L., Cliff, S. S., Reid, E. A., Livingston, J. M., Meier, M. M., Dubovik, O., and Tsay, S.: Comparison of size and morphological measurements of coarse mode dust particles from Africa, J. Geophys. Res. Atmospheres, 108, 2002JD002485, https://doi.org/10.1029/2002JD002485, 2003.

Reid, J. S., Reid, E. A., Walker, A., Piketh, S., Cliff, S., Al Mandoos, A., Tsay, S.-C., and Eck, T. F.: Dynamics of southwest Asian dust particle size characteristics with implications for global dust research, J. Geophys. Res. Atmospheres, 113,
890 https://doi.org/10.1029/2007JD009752, 2008.

Rosenfeld, D., Rudich, Y., and Lahav, R.: Desert dust suppressing precipitation: A possible desertification feedback loop, Proc. Natl. Acad. Sci., 98, 5975–5980, https://doi.org/10.1073/pnas.101122798, 2001.

Saito, M. and Yang, P.: Advanced Bulk Optical Models Linking the Backscattering and Microphysical Properties of Mineral Dust Aerosol, Geophys. Res. Lett., 48, 2021.

895 Saito, M. and Yang, P.: Generalization of Atmospheric Nonspherical Particle Size: Interconversions of Size Distributions and Optical Equivalence, J. Atmospheric Sci., 79, 3333–3349, https://doi.org/10.1175/JAS-D-22-0086.1, 2022.

Saito, M. and Yang, P.: Quantifying the Impact of the Surface Roughness of Hexagonal Ice Crystals on Backscattering Properties for Lidar-Based Remote Sensing Applications, Geophys. Res. Lett., 50, e2023GL104175, https://doi.org/10.1029/2023GL104175, 2023.

900 Saito, M., Yang, P., Ding, J., and Liu, X.: A Comprehensive Database of the Optical Properties of Irregular Aerosol Particles for Radiative Transfer Simulations, J. Atmospheric Sci., 78, 2089–2111, https://doi.org/10.1175/JAS-D-20-0338.1, 2021.

Schuster, G. L., Dubovik, O., and Holben, B. N.: Angstrom exponent and bimodal aerosol size distributions, J. Geophys. Res. Atmospheres, 111, https://doi.org/10.1029/2005JD006328, 2006.

Seifert, P., Ansmann, A., Mattis, I., Wandinger, U., Tesche, M., Engelmann, R., Müller, D., Pérez, C., and Haustein, K.:
905 Saharan dust and heterogeneous ice formation: Eleven years of cloud observations at a central European EARLINET site, J. Geophys. Res. Atmospheres, 115, https://doi.org/10.1029/2009JD013222, 2010.

Tegen, I. and Lacis, A. A.: Modeling of particle size distribution and its influence on the radiative properties of mineral dust aerosol, J. Geophys. Res. Atmospheres, 101, 19237–19244, https://doi.org/10.1029/95JD03610, 1996.

Tegen, I., Lacis, A. A., and Fung, I.: The influence on climate forcing of mineral aerosols from disturbed soils, Nature, 380,
910 419–422, https://doi.org/10.1038/380419a0, 1996.

Tesche, M., Ansmann, A., Müller, D., Althausen, D., Engelmann, R., Freudenthaler, V., and Groß, S.: Vertically resolved separation of dust and smoke over Cape Verde using multiwavelength Raman and polarization lidars during Saharan Mineral Dust Experiment 2008, J. Geophys. Res. Atmospheres, 114, https://doi.org/10.1029/2009JD011862, 2009.

Tesche, M., Kolgotin, A., Haarig, M., Burton, S. P., Ferrare, R. A., Hostetler, C. A., and Müller, D.: 3+2 + *X*: what is the most
useful depolarization input for retrieving microphysical properties of non-spherical particles from lidar measurements using
the spheroid model of Dubovik et al. (2006)?, Atmospheric Meas. Tech., 12, 4421–4437, https://doi.org/10.5194/amt-12-4421-
2019, 2019.

Uematsu, M., Duce, R. A., Prospero, J. M., Chen, L., Merrill, J. T., and McDonald, R. L.: Transport of mineral aerosol from
Asia Over the North Pacific Ocean, J. Geophys. Res. Oceans, 88, 5343–5352, https://doi.org/10.1029/JC088iC09p05343,
1983.

Veselovskii, I., Dubovik, O., Kolgotin, A., Lapyonok, T., Di Girolamo, P., Summa, D., Whiteman, D. N., Mishchenko, M.,
and Tanré, D.: Application of randomly oriented spheroids for retrieval of dust particle parameters from multiwavelength lidar
measurements, J. Geophys. Res. Atmospheres, 115, https://doi.org/10.1029/2010JD014139, 2010.

Veselovskii, I., Goloub, P., Podvin, T., Bovchaliuk, V., Derimian, Y., Augustin, P., Fourmentin, M., Tanre, D., Korenskiy,
M., Whiteman, D. N., Diallo, A., Ndiaye, T., Kolgotin, A., and Dubovik, O.: Retrieval of optical and physical properties of
African dust from multiwavelength Raman lidar measurements during the SHADOW campaign in Senegal, Atmospheric
Chem. Phys., 16, 7013–7028, https://doi.org/10.5194/acp-16-7013-2016, 2016.

Veselovskii, I., Hu, Q., Goloub, P., Podvin, T., Korenskiy, M., Pujol, O., Dubovik, O., and Lopatin, A.: Combined use of Mie–
Raman and fluorescence lidar observations for improving aerosol characterization: feasibility experiment, Atmospheric Meas.
Tech., 13, 6691–6701, https://doi.org/10.5194/amt-13-6691-2020, 2020.

Veselovskii, I., Hu, Q., Goloub, P., Podvin, T., Barchunov, B., and Korenskii, M.: Combining Mie–Raman and fluorescence
observations: a step forward in aerosol classification with lidar technology, Atmospheric Meas. Tech., 15, 4881–4900,
https://doi.org/10.5194/amt-15-4881-2022, 2022.

Volten, H., Muñoz, O., Rol, E., de Haan, J. F., Vassen, W., Hovenier, J. W., Muinonen, K., and Nousiainen, T.: Scattering
matrices of mineral aerosol particles at 441.6 nm and 632.8 nm, J. Geophys. Res. Atmospheres, 106, 17375–17401,
https://doi.org/10.1029/2001JD900068, 2001.

Vouk, V.: Projected Area of Convex Bodies, Nature, 162, 330–331, https://doi.org/10.1038/162330a0, 1948.

Wandinger, U., Freudenthaler, V., Baars, H., Amodeo, A., Engelmann, R., Mattis, I., Groß, S., Pappalardo, G., Giunta, A.,
D'Amico, G., Chaikovsky, A., Osipenko, F., Slesar, A., Nicolae, D., Belegante, L., Talianu, C., Serikov, I., Linné, H., Jansen,
F., Apituley, A., Wilson, K. M., De Graaf, M., Trickl, T., Giehl, H., Adam, M., Comerón, A., Muñoz-Porcar, C.,
Rocadenbosch, F., Sicard, M., Tomás, S., Lange, D., Kumar, D., Pujadas, M., Molero, F., Fernández, A. J., Alados-Arboledas,
L., Bravo-Aranda, J. A., Navas-Guzmán, F., Guerrero-Rascado, J. L., Granados-Muñoz, M. J., Preißler, J., Wagner, F., Gausa,
M., Grigorov, I., Stoyanov, D., Iarlori, M., Rizi, V., Spinelli, N., Boselli, A., Wang, X., Lo Feudo, T., Perrone, M. R., De
Tomasi, F., and Burlizzi, P.: EARLINET instrument intercomparison campaigns: overview on strategy and results,
Atmospheric Meas. Tech., 9, 1001–1023, https://doi.org/10.5194/amt-9-1001-2016, 2016.

Whitby, K. T.: THE PHYSICAL CHARACTERISTICS OF SULFUR AEROSOLS, in: Sulfur in the Atmosphere, edited by:
Husar, R. B., Lodge, J. P., and Moore, D. J., Pergamon, 135–159, https://doi.org/10.1016/B978-0-08-022932-4.50018-5, 1978.

Yang, P. and Liou, K. N.: Geometric-optics–integral-equation method for light scattering by nonspherical ice crystals, Appl
Opt, 35, 6568–6584, https://doi.org/10.1364/AO.35.006568, 1996.

Yang, P., Ding, J., Panetta, R. L., Liou, K.-N., Kattawar, G. W., and Mishchenko, M. I.: ON THE CONVERGENCE OF
NUMERICAL COMPUTATIONS FOR BOTH EXACT AND APPROXIMATE SOLUTIONS FOR ELECTROMAGNETIC

SCATTERING BY NONSPHERICAL DIELECTRIC PARTICLES (INVITED REVIEW), Prog. Electromagn. Res., 164, 27–61, https://doi.org/10.2528/PIER18112810, 2019.

955 Yu, H., Chin, M., Yuan, T., Bian, H., Remer, L. A., Prospero, J. M., Omar, A., Winker, D., Yang, Y., Zhang, Y., Zhang, Z., and Zhao, C.: The fertilizing role of African dust in the Amazon rainforest: A first multiyear assessment based on data from Cloud-Aerosol Lidar and Infrared Pathfinder Satellite Observations, Geophys. Res. Lett., 42, 1984–1991, https://doi.org/10.1002/2015GL063040, 2015.